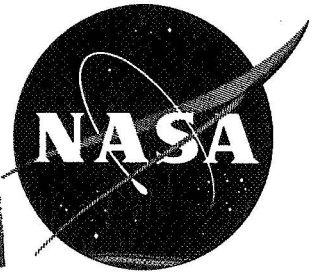

TECHNICAL MEMORANDUM

X-2

JET EFFECTS ON THE BASE, AFTERBODY, AND TAIL REGIONS OF A TWIN-ENGINE AIRPLANE MODEL WITH HIGH AND LOW HORIZONTAL-TAIL LOCATIONS

By Edwin E. Lee, Jr., Willard E. Foss, Jr.,
and Jack F. Runckel

Langley Research Center
Langley Field, Va.

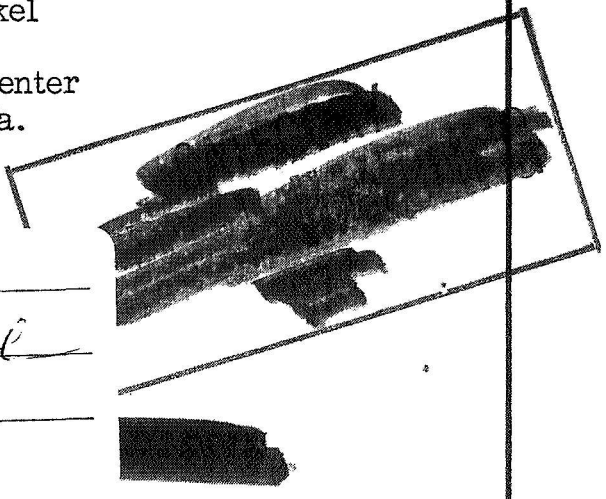

NATIONAL AERONAUTICS AND SPACE ADMINISTRATION
WASHINGTON
August 1959

NATIONAL AERONAUTICS AND SPACE ADMINISTRATION

TECHNICAL MEMORANDUM X-2

JET EFFECTS ON THE BASE, AFTERBODY, AND TAIL REGIONS OF A TWIN-ENGINE AIRPLANE MODEL WITH HIGH AND LOW HORIZONTAL-TAIL LOCATIONS*

By Edwin E. Lee, Jr., Willard E. Foss, Jr., and Jack F. Runckel

SUMMARY

An investigation of the jet-interference effects associated with a twin-engine fighter-airplane model incorporating auxiliary air flow, nonafterburning and afterburning nozzle geometry, and high and low horizontal-tail locations has been conducted in the Langley 16-foot transonic tunnel by using hydrogen peroxide gas generators to simulate the hot turbojet exhausts. Base pressures and drag, afterbody pressures, temperatures, and drag, horizontal-tail pressures, and fuselage-tail lift and pitching moments are presented for various conditions within a range of test variables, including Mach numbers from 0.80 to 1.05, angles of attack from 0° to 12°, and jet-pressure ratios from jet off to 7.

The results indicate that discharging auxiliary air from ports located in the side of the fuselage forward of the engine shrouds caused an increase in base drag near an angle of attack of 8° at high subsonic speeds. Jet operation with afterburning nozzles increased the base pressures in comparison to those obtained with the nonafterburning nozzles and reduced the drag of the basic model (high tail) at all pressure ratios and Mach numbers investigated. Lowering the horizontal tail from the vertical stabilizer to the fuselage overhang resulted in an unstable fuselage-tail combination and in jet-induced nose-up pitching moments, which were not experienced by the high-tail configurations.

INTRODUCTION

An investigation of the jet-interference effects on a model of a twin-engine fighter airplane with an overhanging fuselage has been conducted in the Langley 16-foot transonic tunnel. The effects of fuselage geometry modifications and nonafterburning jet operation on the fuselage pressures and the drag and stability of this airplane configuration were reported in references 1 and 2. The model configurations of these references incorporated high horizontal-tail surfaces which were found to be unaffected by the jet exhausts (ref. 3). It has been shown, however, (refs. 3 and 4) that positioning the horizontal-tail surfaces in close proximity to engine exits can result in appreciable jet interference. This report presents the results of an investigation of the basic models of references 1 and 2 in which the jet-to-horizontal-tail vertical and longitudinal spacing were varied in order to study the influence of tail height on stability and the jet-interference problems associated with the low-tail position.

Other variables examined herein include the effect of discharging auxiliary (engine compartment cooling) air flow from the fuselage ahead of the jet exits, and the effects of engine nozzle size (simulated nonafterburning and afterburning geometry) and single-engine operation on model surface pressures and temperatures. Engine base, afterbody, and horizontal-tail pressures, afterbody temperatures, and fuselage-tail lift and pitching-moment coefficients were measured at Mach numbers from 0.80 to 1.05 and angles of attack ranging from 0° to 12°. Jet operation at pressure ratios from no flow to 7 was simulated by hydrogen peroxide gas generators of the type described in reference 5. The average Reynolds number, based on the wing mean aerodynamic chord, was approximately 5.0×10^6.

SYMBOLS

A	axially projected area, sq ft
A_b	base area, $A_e - A_j$, sq ft
$\bar{c}$	mean aerodynamic chord of basic wing (fig. 2), ft
$C_{D,b}$	base drag coefficient, $\bar{C}_{p,b} \frac{A_b}{S}$
ΔC_D	jet-induced pressure drag, $\frac{1}{S} \int \Delta C_{p,j} \, dA$

$\Delta C_{D,j}$	approximate jet-induced drag on complete model, $\Delta C_{D,a} + \Delta C_{D,b}$
C_L	fuselage-tail lift coefficient, $\frac{F_L}{q_\infty S}$
C_m	fuselage-tail pitching-moment coefficient, $\frac{M_Y}{q_\infty S \bar{c}}$
$\Delta C_{m,j}$	jet-induced fuselage-tail pitching-moment coefficient, $(C_m)_{\text{jet on}} - (C_m)_{\text{jet off}}$
$c_{n,t}$	horizontal-tail section normal-force coefficient
$\frac{\Delta c_{n,t}}{\Delta \alpha}$	horizontal-tail section effectiveness parameter (evaluated between $\alpha = 0^\circ$ and 4°)
C_p	pressure coefficient, $\frac{p_l - p_\infty}{q_\infty}$
$\bar{C}_{p,b}$	average base-pressure coefficient
$\Delta C_{p,j}$	jet-induced pressure coefficient, $(C_p)_{\text{jet on}} - (C_p)_{\text{jet off}}$
d	diameter, in.
i_t	horizontal-tail incidence angle measured at root chord with respect to fuselage reference line, deg
F_L	fuselage-tail lift, lb
M	Mach number
M_Y	fuselage-tail pitching moment about $0.29\bar{c}$, ft-lb
p	static pressure, lb/sq ft
p_t	total pressure, lb/sq ft
q	dynamic pressure, lb/sq ft
S	basic wing area (see fig. 2), sq ft

T	total temperature, °F
t	measured model surface temperature, °F
x	longitudinal distance from shroud exit or horizontal-tail leading edge, positive rearward, in.
y	lateral distance from model plane of symmetry, positive to right looking forward, in.
z	vertical distance from plane containing jet center lines, positive upward, in.
α	angle of attack of fuselage reference line (fig. 2), deg
β	boattail angle, deg
δ	nozzle-to-shroud exit spacing, in.
θ	temperature parameter, $t_l - T_\infty / T_j - T_\infty$
ϕ	meridian angle at engine base (fig. 5), deg

Subscripts:

a	afterbody
b	base
e	shroud exit
j	jet
l	local
∞	free stream

APPARATUS AND METHODS

Wind-Tunnel and Support System

The investigation was conducted in the Langley 16-foot transonic tunnel which is a single-return atmospheric wind tunnel having a slotted test section and provision for air exchange.

The support system, shown in figures 1 and 2, consisted of a strut-mounted bifurcate sting which held the model by the wing tips near the center line of the tunnel. The forces and moments of the fuselage-tail combination were measured by an internal strain-gage balance supported from the wing panels, which were an integral part of the support system. A clearance gap, filled with a flexible sponge material, was maintained between the fuselage and the wing panels to permit deflection of the balance by the fuselage-tail assembly. In order to provide adequate strength in the support system, the wing span was reduced slightly as shown in figure 2.

Model

L 2 0 5

The model was constructed entirely of steel with the exception of plastic overlays on portions of the wing surfaces and the nose-canopy section. The wing-root inlets were closed and faired to streamline contours without altering the wing plan form in this region. Two hydrogen peroxide jet-simulator units similar to those shown in figure 7(a) of reference 5 were supported internally from the wing panels and independently of the fuselage-tail assembly. Each unit generated a hot exhaust with a stagnation temperature of approximately 1,360° F.

Four principal model configurations were investigated, and the essential features of each are indicated in table I. Configurations I and II incorporated the basic airplane fuselage with the horizontal tail mounted in a high and low position, respectively. Configurations III and IV utilized the same high-tail and low-tail surfaces and mounting positions but the fuselage was modified (ref. 2) by extending the engine compartment section and displacing the engine shrouds and jet exits rearward along the jet center lines. Behind the jet exits, the afterbody geometry was similar to that of the basic fuselage. Configuration I(a) of table I was identical to configuration I of reference 2. Configuration III(a) was identical to the basic configuration of reference 1 and to configuration III of reference 2.

The two horizontal-tail positions investigated are shown in figures 1 and 3 and the physical dimensions of the complete basic model (configuration I) and the low horizontal tail are given in figure 2. Physically, the low tail consisted of the panels used in the high position, and adapter fillets (see fig. 3) machined to fit the contours of the fuselage overhang. Dimensions pertaining to the location of the horizontal tail and the jet exits for the principal configurations appear in figure 4.

Both nonafterburning and afterburning nozzle geometry was incorporated in the investigation (table I) and the geometrical details of

the exit configurations are shown in figure 5. Mass discharge coefficients ranged from 0.92 to 0.99 and indicated typical sonic nozzle operation. Auxiliary air flow, which simulated engine compartment cooling air, was also included in various configurations (table I). Air entered the model through two flush inlets positioned low on the sides of the fuselage (figs. 6 and 7) and discharged either through base bleed slots in the fuselage-shroud clearance gaps or through the fuselage exits (simulated louvers) located above and ahead of the shrouds or through both outlet systems simultaneously (see fig. 7), depending upon the model configuration. No secondary air flow through the engine bases was considered in the investigation. Flexible seals were installed between the simulator tailpipes and the engine shrouds on all configurations.

Tests

In general, the present investigation was conducted at Mach numbers ranging from 0.80 to 1.05; however, most of the data presented herein were taken at the specific values of 0.85, 0.95, 1.00, and 1.05. At subsonic speeds the angle of attack generally ranged from 0° to 12°. At supersonic speeds, the maximum angle was confined to 8° or less by stress limitations on the model and support system. At each Mach number and angle of attack, the jet-simulator units were operated through a cycle of jet-pressure ratios of 1, 3, 5, and 1, where a value of 1 has been assigned to the initial and final jet-off conditions. At Mach numbers of 1.00 and 1.05 a jet-pressure ratio of 7 was included in the cycle. The Reynolds number, based on the mean aerodynamic chord of the basic wing (fig. 2), varied from approximately 4.7×10^6 to 5.5×10^6.

Instrumentation

For all configurations tested, the left engine base, the left side of the afterbody, and the left horizontal-tail panel were instrumented with pressure orifices at the locations shown in figures 4 and 5. In figure 4, the afterbody pressure instrumentation is shown for rows at $\phi = 30^\circ$ and 90° and at the fuselage bottom center line. A limited number of thermocouples, peened into the model surface, were also included on the afterbody in the rows at $\phi = 30^\circ$ and 60°. Coordinates of the individual orifice and thermocouple locations are given for the two fuselage configurations in tables II and III. The horizontal-tail orifices were located at the leading edge, and on the upper and lower surface at 5 percent of the local chord, and at every 10 percent thereafter (fig. 4).

All afterbody pressure measurements were taken by electrical pressure transducers. During jet operation, certain horizontal-tail pressures were obtained by transducer measurements only, but during jet-off conditions additional data were obtained with mercury manometers. Fuselage-tail forces and moments were measured by a six-component strain-gage balance, and the model angle of attack was determined with a pendulum-type strain-gage attitude indicator mounted in the fuselage. (See fig. 2.) Transducer, thermocouple, and balance outputs were read on recording oscillographs and manometer data were photographically recorded.

Data Reduction and Accuracies

The data read from oscillograph records and photographic film were converted to punch cards and reduced to coefficient form by machine computation. The data, as presented, are accurate to within the following limits:

M_∞	±0.005
α, deg	±0.2
C_p	±0.02
$p_{t,j}/p_\infty$	±0.2
$C_{D,a}$	±0.0005
$C_{D,b}$	±0.0003
$c_{n,t}$	±0.02

The drag-coefficient accuracies quoted above apply to values obtained by pressure integrations. In the particular phase of the overall investigation reported herein, the fuselage-tail drag measurements were impaired by balance temperature compensation problems. (See ref. 1.) Consequently, only fuselage-tail lift and pitching-moment data are presented. Since these balance data are necessarily qualitative, no specific accuracies can be quoted.

The effects of support-system interference on the data have been discussed previously in references 1 and 6. It is believed that interference effects on any given configuration are small and become insignificant with regard to configuration comparisons.

RESULTS

Results of the investigation are presented for the three regions of the model affected by jet operation: the engine base region, the

afterbody (lower portion of the fuselage overhang), and the horizontal tail. For each of these regions the effects of jet-pressure ratio, auxiliary air discharge, engine nozzle configuration, angle of attack, Mach number, and model configuration will generally be discussed.

Data obtained from base-pressure measurement are presented in figures 8 to 13. The effects of auxiliary air flow on base pressures and base drag are given in figures 8 and 9, the effect of model angle of attack on base pressures and drag is shown in figures 10 and 11, and the influence of engine exit nozzle size is illustrated in figures 12 and 13.

Information on the afterbody region is given in figures 14 to 21. Effects of auxiliary air flow on afterbody pressures and temperatures are presented in figures 14, 15, and 16. Figure 17 shows the effect of single-engine operation on afterbody pressure distributions, and the variation in afterbody pressures with angle of attack is shown in figure 18. The influence of jet exit nozzle size on the afterbody pressures, drag, and temperatures is illustrated in figures 19, 20, and 21.

Results for the models with high and low horizontal tails are presented in figures 22 to 33. The alteration of afterbody pressure distributions due to the presence of the low tail is given in figure 22. Horizontal-tail section pressure distributions at angles of attack are presented in figure 23, and the variation with Mach number appears in figure 24 for jet-off conditions. Jet effects on the tail pressure distribution are shown in figures 25 and 26 and the effect of the spacing of the jet exit to the horizontal tail in figure 27. Figures 28 and 29 show the variation of horizontal-tail section normal-force coefficient with angle of attack with jets off and on. These results are summarized over the Mach number range in figure 30. The manner in which the tail location affected the model fuselage-tail lift and pitching-moment coefficients is illustrated in figures 31 to 33.

DISCUSSION

Engine Base Region

References 1 and 2 have shown the engine base region of the airplane configuration reported herein to be the source of considerable drag because of the aspirating effect of the primary jets. The effect of auxiliary air flow on the pressures in this region is of interest from the standpoint of possible alleviation of this undesirable drag characteristic particularly at cruising conditions ($M \approx 0.85$; $\alpha \approx 4^{\circ}$;

$p_{t,j}/p_\infty \approx 3.0$). Figures 8 and 9 show, however, that, regardless of the outlet system used, the effects of auxiliary air flow were small although generally favorable at an angle of attack of 4° for all Mach numbers and pressure ratios. When auxiliary air was discharged from the fuselage exits only (configuration I(c)), a considerable decrease in base pressure (fig. 10) and corresponding increase in base drag (fig. 11) occurred at angles of attack of 6° to 8° at high subsonic speeds with and without jet operation. This variation in the base conditions apparently resulted from changes in the flow over the top of the shrouds caused by the auxiliary air discharging from the fuselage exits.

Increasing the jet-to-base diameter ratio from 0.72 (nonafterburning nozzle) to 0.94 (afterburning nozzle) produced large increases in base-pressure coefficient above a jet-pressure ratio of 3 at all Mach numbers for both fuselage configurations. (See fig. 12.) This increase in base pressures with increasing jet-to-base diameter ratio is similar to results reported in reference 7 and resulted from the interaction of the jets with the external flow at a lower pressure ratio. In figure 13, the reductions in base drag associated with the afterburning nozzle configuration resulted from both an increase in base pressure, and a decrease of approximately 80 percent in base area.

Afterbody Region

At subsonic speeds, auxiliary air flow (fig. 14) generally had small effects on the afterbody pressures, both with and without jet operation. Configurations employing base bleed experienced the largest effects, and at supersonic speeds (fig. 15) only slight increases in pressure near the exits were noted.

The qualitative effects of auxiliary air flow on the afterbody surface temperatures are presented in figure 16 for typical cruise conditions. Considerable reductions in afterbody temperatures were achieved with configurations using base bleed.

The effect of single-engine operation, shown in figure 17, was to decrease the pressure on the left side of the afterbody when the right simulator was inoperative. This effect was largest on the lower portion of the afterbody where the pressurizing influence of the right engine would be most pronounced during normal twin-engine operation.

Angle of attack had very little influence on afterbody pressures (fig. 18) with or without jet operation. At model attitudes as high as 10° the pressures over the rear of the afterbody were increased slightly over those at 0°.

Incremental afterbody pressures induced by jet operation are shown in figure 19 for the basic model configuration with both types of nozzles. As reported previously in reference 2, the nonafterburning nozzles produced favorable jet effects at subsonic cruise conditions. The afterburning nozzles produced favorable effects at all Mach numbers and jet-pressure ratios. The induced pressures were less favorable for the larger nozzle at high pressure ratios because of the reduced clearance between the larger jet and the afterbody surface (aspirating effect, ref. 2). This result is indicated in the jet-induced afterbody drag values of figure 20 at pressure ratios from 3 to 5. Because of the improvement in base conditions associated with the afterburning nozzle, the combined effect on base and afterbody $\Delta C_{D,j}$ was more favorable in the afterburning case. Since the high tail of these configurations was unaffected by jet operation, as will be shown subsequently, the values of $\Delta C_{D,j}$ are indicative of the overall effects on the model and indicate that afterburning nozzle geometry had a favorable influence on the drag of the basic airplane configuration.

Qualitative temperature data measured on the surface of the heavy steel afterbodies are shown in figure 21. The reduced spacing between the jet and afterbody surface associated with the afterburning nozzle resulted in higher temperatures than those produced by the nonafterburning nozzle. The continuous temperature rise along the row at $\phi = 30^{\circ}$ for the afterburning nozzle is consistent with unpublished shadowgraph pictures which show that considerable vertical spreading of the jets occurred and that the exhaust gases may have been impinging on the fuselage.

The influence of the low horizontal tail on the afterbody pressures at $\phi = 30^{\circ}$ is illustrated in figure 22. Negative pressure increments, corresponding to the acceleration of the flow around the root fillets, were induced on the afterbody. The increments tended to increase in magnitude with increasing jet-pressure ratio, presumably because of entrainment.

Horizontal-Tail Region

The following discussion of the horizontal-tail loading pertains to the single row of orifices located directly above the jet center line on the high tail and slightly outboard of this position on the low tail as shown in figure 4. In comparing the data for the two tail positions, the corresponding geometry changes (fig. 2) must also be considered, particularly the -2.6° incidence of the low tail.

The jet-off pressure data of figure 23 typify the variation in tail loading with vertical position and changes in fuselage geometry. Parts (a) and (b) of figure 23 provide a comparison of the high and low tails in the presence of the basic fuselage and show that the low tail experienced very little change in loading with model angle of attack due to the predominance of the fuselage-wing wake. The effect of fuselage geometry on the low tail can be seen by comparing parts (b) and (c) of figure 23, which show that the rearward displacement of the engine shrouds caused slight changes in the leading-edge pressures corresponding to small downward changes in the local flow direction. (See ref. 2.) Figure 24 indicates that the reduced loading on the low tail attributed to the fuselage-wing wake existed over the Mach number range.

The effect of jet operation on the horizontal tail is illustrated in figures 25 and 26 for the high and low positions, respectively. The jets had no effect on the high tail (see ref. 3); however, in the low position the tail experienced a general decrease in lower surface pressures corresponding to the aspirating influence of the jets. Reducing the engine exit-to-tail spacing increased the aspirating effect, particularly at the higher pressure ratios. (See fig. 27.)

Tail-section normal-force coefficients of configurations I, II, and III, obtained from integration of the section pressure distributions, are shown plotted against angle of attack for several Mach numbers in figure 28. As noted previously, the high tail experienced no jet effects. Extending the engine compartments (configuration III) reduced the normal force on the high tail slightly. This effect, attributed to downward changes in the local flow direction caused by the displaced shrouds, was generally present over the angle-of-attack range but diminished with Mach number. The difference in the jet-off normal-force levels of the high- and low-tail positions, evident in figure 28, is primarily due to the negative incidence setting of the low tail. The reduced slope of the low-tail curves is, however, the result of positioning the tail in the fuselage-wing wake.

The aspirating effect of the jets on the lower surface pressures of the low tail is indicated in the curves of figure 28 by the reduction in normal force with increasing pressure ratio. At a given pressure ratio the jet-induced loads remained relatively constant over most of the Mach number and angle-of-attack range.

The effect of jet-exit location on the low horizontal tail is illustrated in figure 29. Again, as in the case of the high tail, the fuselage modification reduced the normal force, but the amount of the reduction was considerably larger for the low tail. This result might be expected since the geometry changes would exert a stronger influence

on the flow field in the immediate vicinity of the fuselage. Displacing the jet exits rearward approximately doubled the effects of jet operation on the low tail at the lower angles of attack.

The tail-section effectiveness parameters for the various configurations are shown in figure 30. These data are based on model angle of attack and were evaluated from the curves of the section normal force plotted against model angle of attack between angles of 0° and 4°. The results show that lowering the horizontal tail resulted in considerable loss in effectiveness over the entire Mach number range.

The influence of configuration geometry changes and jet operation on the lift and pitching-moment coefficients of the fuselage-tail combination are illustrated qualitatively by the balance data shown in figures 31 to 33. The variation of these data with angle of attack indicates that lowering the horizontal tail reduced the fuselage-tail lift and made the fuselage-tail combination longitudinally unstable. Fuselage geometry changes, which appeared to have little effect on lift, produced nose-up pitching-moment increments consistent with the influence of the displaced shrouds on the horizontal-tail loading discussed previously. This effect, obtained for both the high- and low-tail positions, was largest for the low-tail position and generally persisted over the Mach number range (fig. 32).

The effect of jet operation on the fuselage-tail pitching moment (fig. 33) was to induce slight nose-down moment increments on the high-tail configurations. Since the high tail was unaffected by jet operation (fig. 28), these increments are directly attributable to the increase in pressure on the afterbody, as shown previously in figure 19 and in references 1 and 2. Previous data have shown, however, that the low tail experienced jet-induced downloads, which increased in severity with increasing pressure ratio, and the corresponding nose-up moments appear in figure 33. It can be seen that the opposing effects on the afterbody and tail tended to compensate near a pressure ratio of 3 but that the tail jet effects predominated as the pressure ratio was increased further. Configuration IV, which represented the most severe jet-tail interference situation from the standpoint of geometry (extended engine compartments, afterburning nozzles, low tail), experienced a sharp moment break at a pressure ratio of 5 at supersonic speeds. This result suggests that the pitching characteristics of this configuration might become somewhat erratic at higher speeds and pressure ratios.

SUMMARY OF RESULTS

An investigation of the effects of jet operation, auxiliary air flow, engine nozzle size, and horizontal-tail position on the aerodynamic

characteristics of a twin-jet fighter-airplane model showed the following results at transonic speeds:

1. Discharging auxiliary air from various outlet systems in the fuselage ahead of the jet exits had little effect on afterbody pressures but reduced afterbody temperatures. Auxiliary air flow had no significant effect on base pressures at low angles of attack; however, near 8°, considerable increases in base drag occurred when air was discharged from the fuselage exits only.

2. Increasing engine nozzle size to simulate the change from non-afterburning to afterburning conditions resulted in more positive base pressures during jet operation, particularly at the higher pressure ratios and Mach numbers. Afterburning nozzle operation caused favorable jet effects on the overall drag of the basic airplane configuration (high tail).

3. Lowering the horizontal tail from a position near the top of the vertical stabilizer to the sides of the fuselage overhang reduced the fuselage-tail lift and made the fuselage-tail combination longitudinally unstable.

4. Jet operation had no effect on the high tail; however, lower surface pressures of the low tail decreased with increasing pressure ratio and resulted in nose-up fuselage-tail moment increments. Reducing the longitudinal spacing between the afterburning nozzle exits and the low horizontal tail resulted in somewhat erratic jet-induced moments at supersonic speeds.

Langley Research Center,
National Aeronautics and Space Administration,
Langley Field, Va., January 19, 1959.

REFERENCES

1. Foss, Willard E., Jr., Runckel, Jack F., and Lee, Edwin E., Jr.: Effects of Boattail Area Contouring and Simulated Turbojet Exhaust on the Loading and Fuselage-Tail Component Drag of a Twin-Engine Fighter-Type Airplane Model. NACA RM L58C04, 1958.

2. Lee, Edwin E., Jr., and Salters, Leland B., Jr.: Effects of Afterbody Shape and Hot Jet Exhausts on Pressures, Temperatures, and Drag of a Twin-Engine Fighter-Airplane Model Having an Overhanging Fuselage. NASA MEMO 12-29-58L, 1959.

3. Swihart, John M., and Crabill, Norman L.: Steady Loads Due to Jet Interference on Wings, Tails, and Fuselages at Transonic Speeds. NACA RM L57D24b, 1957.

4. Jackson, Bruce G.: Free-Flight Transonic Model Investigation of Jet Effects on a Fighter-Type Configuration Employing a Tail Boom and Three Horizontal-Tail Positions. NACA RM L57J31, 1958.

5. Runckel, Jack F., and Swihart, John M.: A Hydrogen Peroxide Turbojet-Engine Simulator for Wind-Tunnel Powered-Model Investigations. NACA RM L57H15, 1957.

6. Norton, Harry T., Jr., and Swihart, John M.: Effect of a Hot-Jet Exhaust on Pressure Distributions and External Drag of Several Afterbodies on a Single-Engine Airplane Model at Transonic Speeds. NACA RM L57J04, 1958.

7. Henry, Beverly Z., Jr., and Cahn, Maurice S.: Preliminary Results of an Investigation at Transonic Speeds To Determine the Effects of a Heated Propulsive Jet on the Drag Characteristics of a Related Series of Afterbodies. NACA RM L55A24a, 1955.

TABLE I.- MODEL CONFIGURATION VARIABLES

Model configuration	Fuselage configuration	Horizontal-tail position*	Primary jets			Auxiliary air flow			
			Nonafterburning nozzles with -		After-burning nozzles	None	Inlets and -		
			Left engine operating	Both engines operating	Both engines operating		Base bleed	Fuselage exits	Fuselage exits and base bleed
I(a)	Basic	High ($x/d_e=3.34$; $z/d_e=3.83$)		x		x			
I(b)				x			x		
I(c)				x				x	
I(d)			x					x	
I(e)				x					x
I(f)					x		x		
II	Basic	Low ($x/d_e=2.17$; $z/d_e=1.55$)			x		x		
III(a)	Extended engine compartments	High ($x/d_e=2.59$; $z/d_e=3.83$)		x		x			
III(b)				x			x		
IV	Extended engine compartments	Low ($x/d_e=1.42$; $z/d_e=1.55$)			x		x		

*Coordinates x/d and z/d are the distances from the jet exit and center line, respectively, to the tail leading edge, measured in the vertical plane through the jet center line.

TABLE II.- COORDINATES OF FUSELAGE THERMOCOUPLES AND PRESSURE ORIFICES FOR CONFIGURATIONS I AND II

Orifice row	Model station	-y, in.	z, in.	x/d_e	Type (a)
Base					
ϕ = 30°	74.90	1.99	1.66	-0.28	t
ϕ = 90°	74.90	1.02	0	-.28	t
ϕ = 120°	74.90	1.28	-.95	-.28	t
ϕ = 180°	74.90	2.94	-1.92	-.28	t
ϕ = 255°	74.90	4.79	-.50	-.28	t
ϕ = 330°	74.90	3.90	1.66	-.28	t
Afterbody					
ϕ = 30°	75.27	1.81	2.18	-0.18	t
	75.89	1.80	1.97	-.03	t
	76.53	1.79	2.02	.13	t
	76.89	1.75	2.07	.22	th
	77.15	1.73	2.09	.29	t
	78.40	1.51	2.29	.60	t
	79.65	1.52	2.47	.91	t
	80.28	1.47	2.55	1.07	th
	80.90	1.42	2.64	1.23	t
	83.40	1.23	2.99	1.85	t
	85.28	1.09	3.23	2.32	th
	85.90	1.05	3.32	2.48	t
	88.40	.87	3.60	3.10	t
	90.29	.74	3.84	3.57	th
	90.91	.71	3.90	3.73	t
	93.40	.54	4.18	4.35	t
	95.90	.37	4.48	4.98	t
	98.41	.20	4.81	5.60	t
	99.02	-.01	4.92	5.76	th
ϕ = 90°	75.89	0.71	0	-0.03	t
	76.53	.71	0	.13	t
	77.16	.63	.01	.29	t
	78.41	.47	.01	.60	t
	79.66	.30	.02	.91	t
	80.90	.14	0	1.23	t
Bottom center line	75.27	0.01	-1.47	-0.18	t
	75.92	0	-1.35	-.02	t
	76.52	0	-1.24	.13	t
	77.17	0	-1.10	.29	t
	78.41	0	-.85	.60	t
	85.91	-.01	2.54	2.48	t

[a] t, transducer; th, thermocouple.

TABLE III.- COORDINATES OF FUSELAGE THERMOCOUPLES AND PRESSURE ORIFICES FOR CONFIGURATIONS III AND IV

Orifice row	Model station	-y, in.	z, in.	x/d_e	Type (a)
Base					
$\phi = 30^\circ$	77.90	1.99	1.66	-0.28	t
$\phi = 90^\circ$	77.90	1.02	0	-.28	t
$\phi = 120^\circ$	77.90	1.28	-.95	-.28	t
$\phi = 180^\circ$	77.90	2.94	-1.92	-.28	t
$\phi = 255^\circ$	77.90	4.79	-.50	-.28	t
$\phi = 330^\circ$	77.90	3.90	1.66	-.28	t
Afterbody					
$\phi = 30^\circ$	78.26	1.73	2.02	-0.19	t
	78.90	1.85	1.87	-.03	t
	79.53	1.80	1.90	.13	t
	79.89	1.77	1.96	.22	th
	80.15	1.75	1.99	.29	t
	81.40	1.64	2.17	.60	t
	82.65	1.54	2.36	.91	t
	83.27	1.49	2.46	1.07	th
	83.90	1.43	2.55	1.23	t
	86.39	1.25	2.93	1.85	t
	88.29	1.05	3.09	2.32	th
	88.91	1.03	3.14	2.48	t
	91.40	.86	3.56	3.10	t
	93.28	.73	3.78	3.57	th
	93.91	.66	3.86	3.73	t
	96.41	.48	4.18	4.35	t
	98.90	.28	4.53	4.98	t
	99.03	0	4.40	5.01	th
$\phi = 90^\circ$	78.89	0.72	-0.06	-0.03	t
	79.52	.71	-.08	.13	t
	80.15	.64	-.07	.29	t
	81.40	.48	-.08	.60	t
	82.65	.33	-.08	.91	t
Bottom center line	78.28	0.01	-1.55	-0.18	t
	78.89	-.01	-1.43	-.03	t
	79.51	0	-1.32	.13	t
	80.15	-.01	-1.19	.29	t
	81.40	-.01	-.93	.60	t
	83.90	-.01	-.28	1.23	t
	88.93	0	2.48	2.48	t

[a] t, transducer; th, thermocouple.

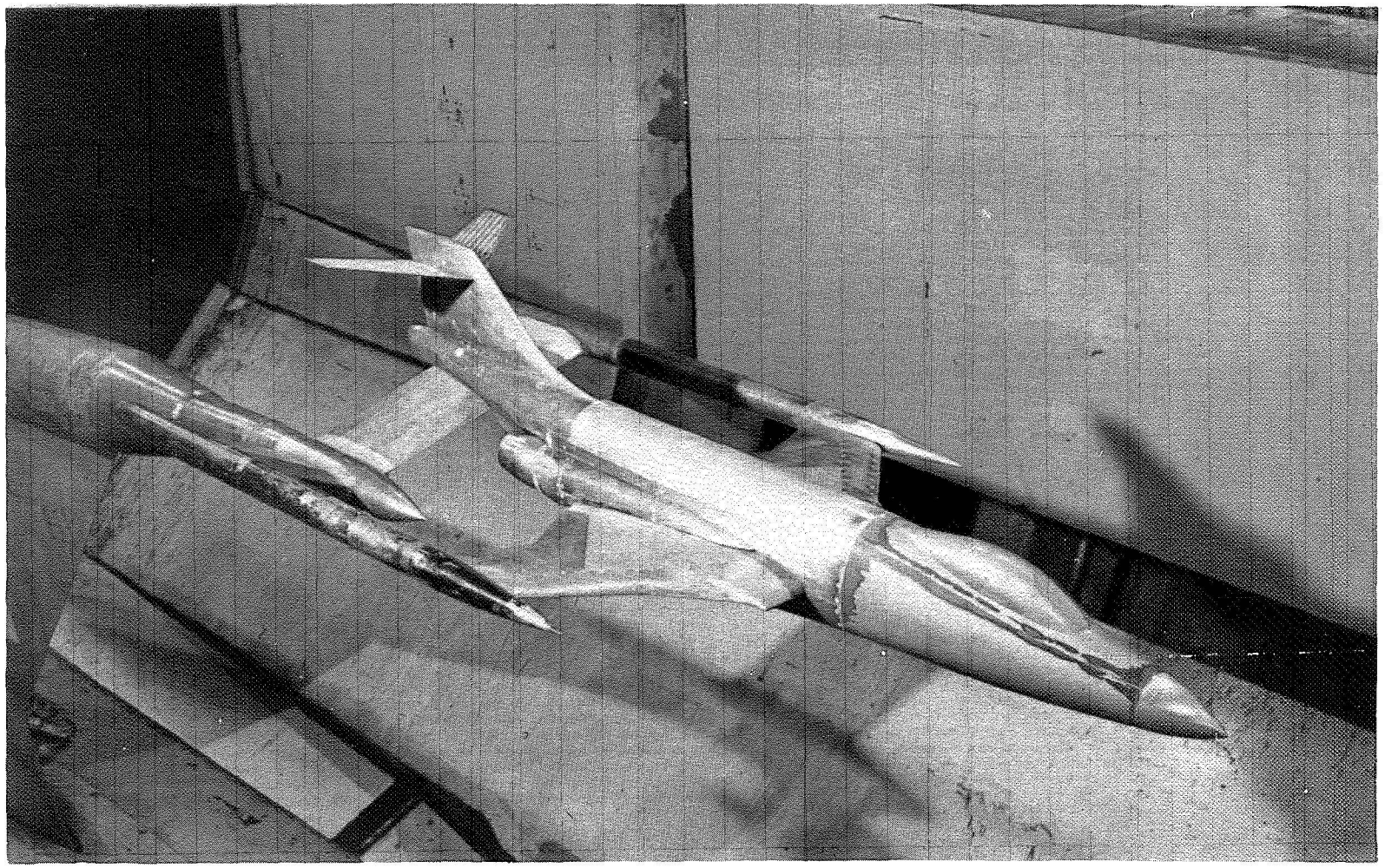

(a) Three-quarter front view. L-95566

Figure 1.- Typical installation of the twin jet-exit model and bifurcate-sting-support system in the tunnel test section.

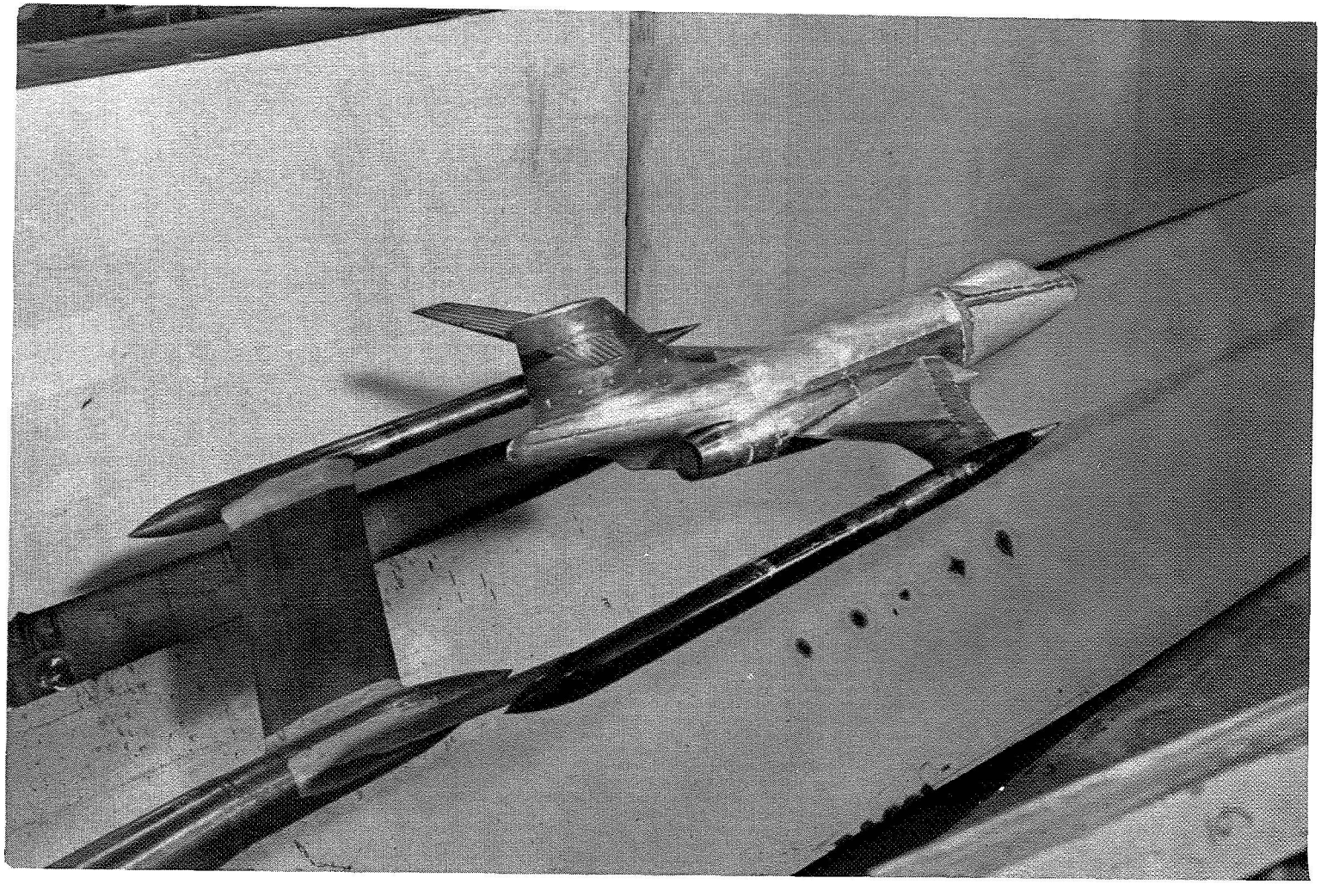

(b) Three-quarter rear view. L-95567

Figure 1.- Continued.

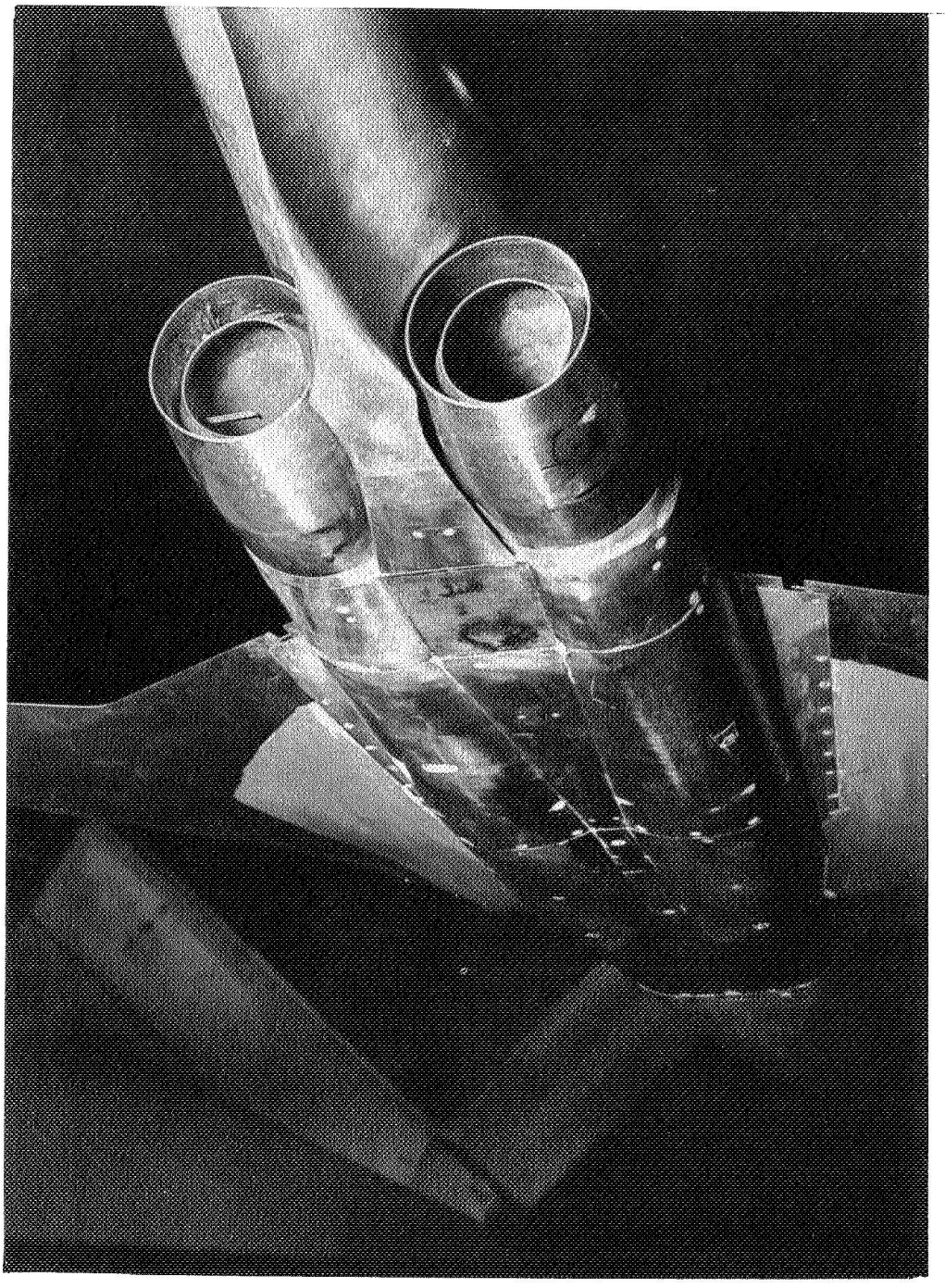

(c) Bottom view of jet exits. L-95565

Figure 1.- Concluded.

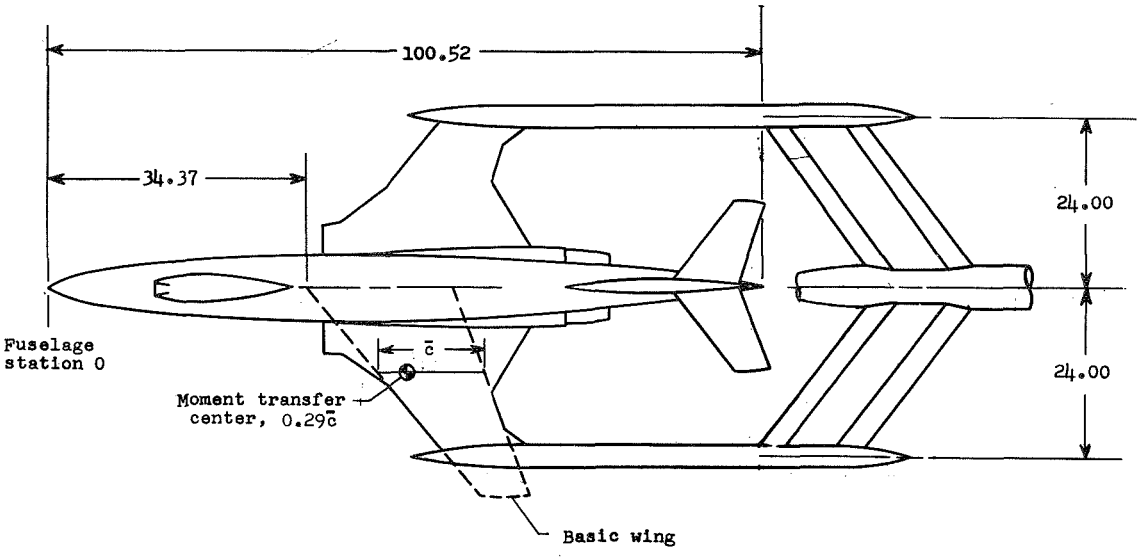

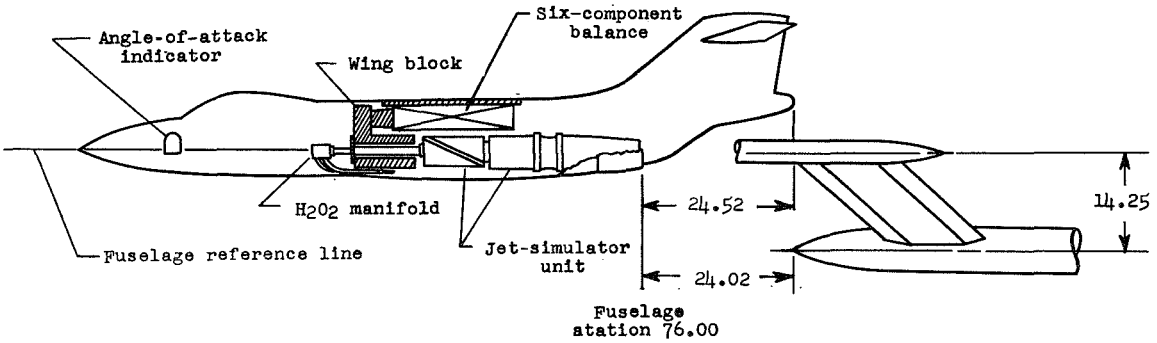

ITEM	WING, BASIC (SHOWN BY DASHED LINES)	HIGH HORIZONTAL TAIL	LOW HORIZONTAL TAIL	VERTICAL TAIL
Area, sq ft	5.75	1.17	1.38	1.18[2]
Span, ft	4.95	1.97	2.09	0.94
Aspect ratio	4.28	3.30	3.17	
Mean aerodynamic chord, ft	1.28	0.62	.71	1.46[2]
Taper ratio	0.28	0.46	.41	
Incidence angle, deg	1.00	0.00	-2.60	
Dihedral angle, deg	0.00	10.00	-15.29	
Sweepback of leading edge, deg	41.12	39.80	45.93	52.00
Sweepback of trailing edge, deg	19.42	20.93	26.94	16.60
Root airfoil section	NACA 65A007[1]	65A007	65A007	65A007
Tip airfoil section	NACA 65A006[1]	65A006	65A006	65A007

1 The wing airfoil sections were modified forward of the 16.04-percent-chord line by extending the chord 5 percent and incorporating 1.67 percent positive camber.
2 Basic, excluding dorsal.

Figure 2.- Dimensional details of the basic model and the low horizontal tail. All dimensions are in inches unless otherwise noted.

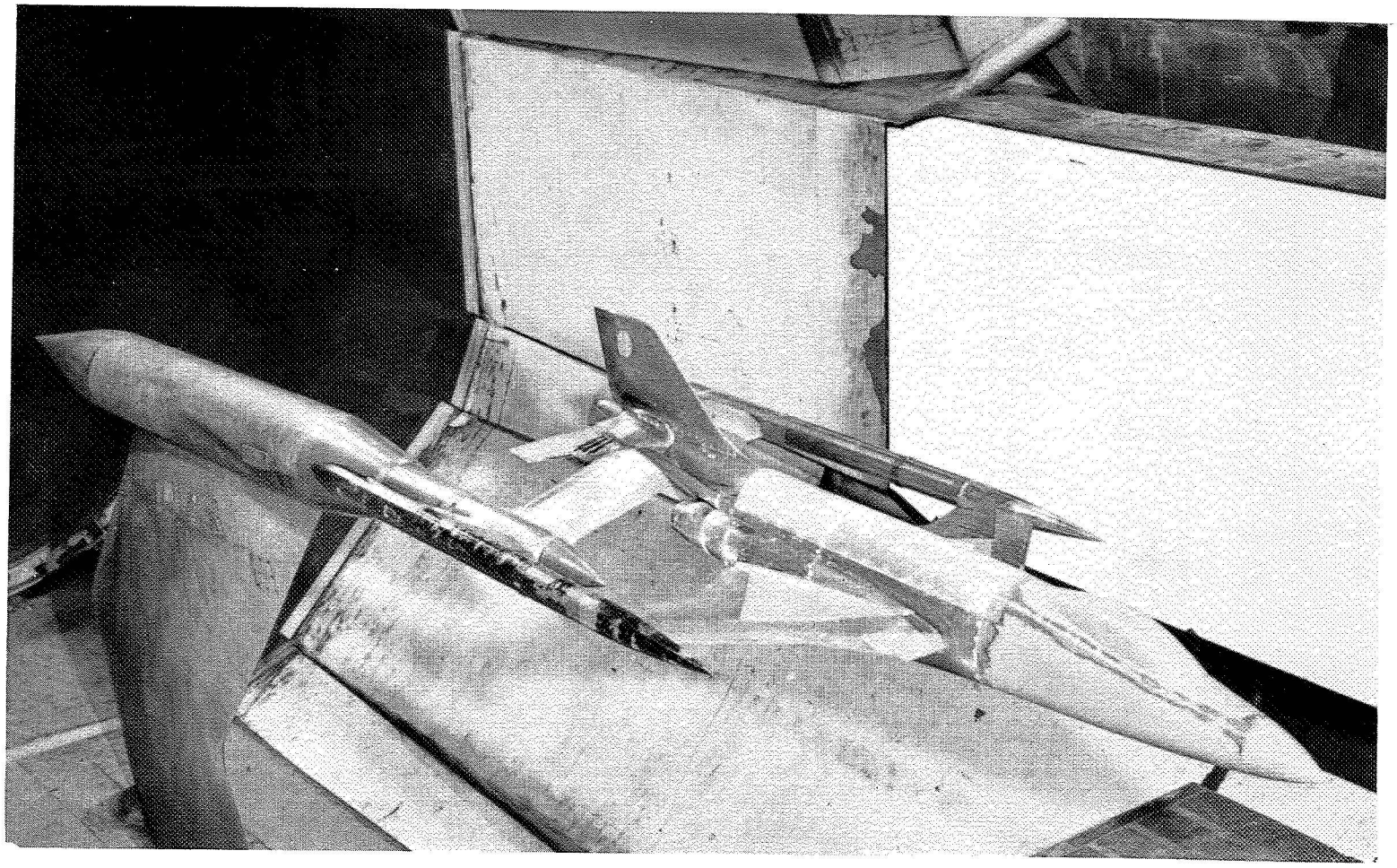

Figure 3.- Model with typical low-horizontal-tail installation. L-94380

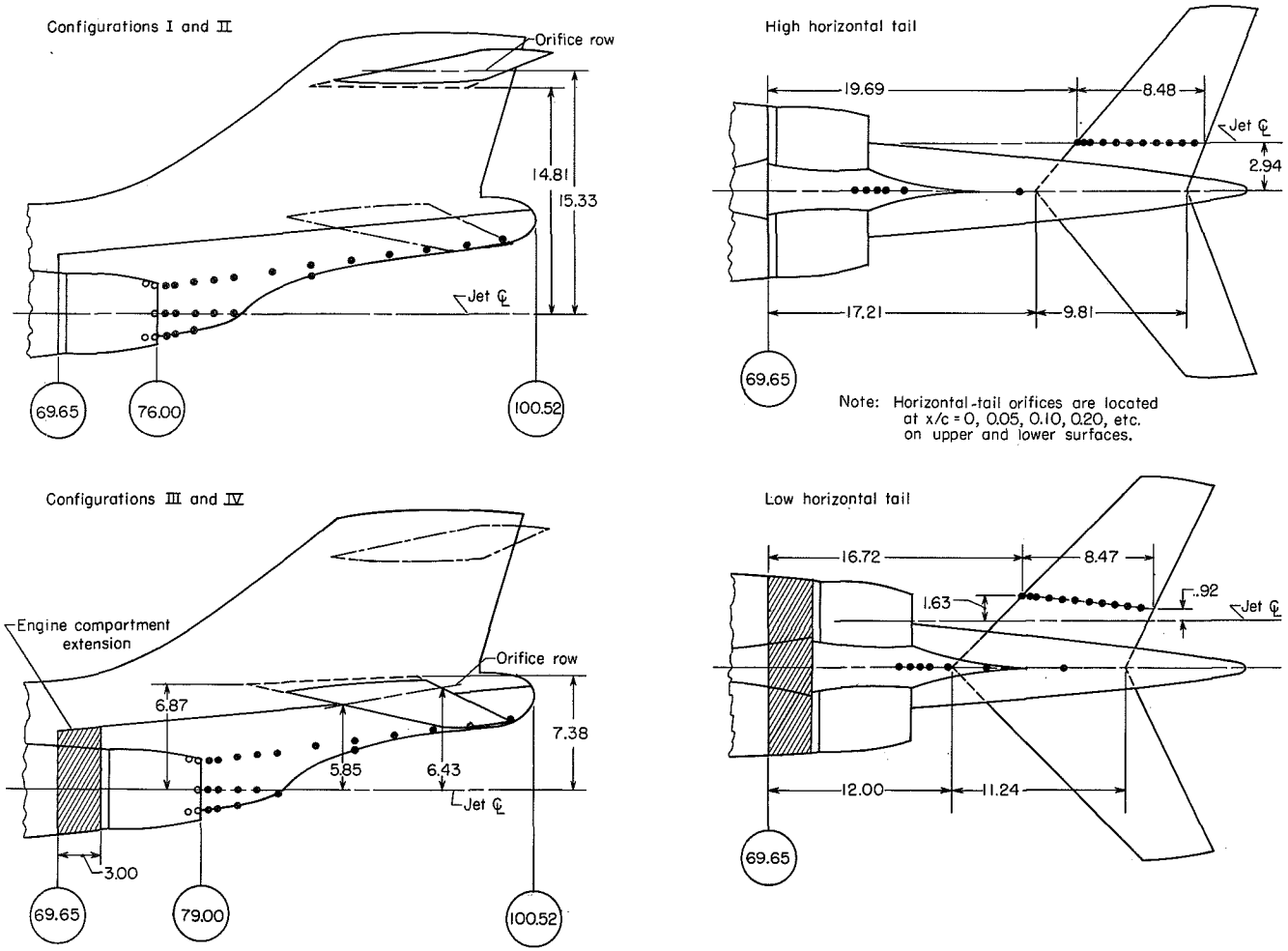

Figure 4.- Sketch showing major configuration changes and general arrangement of pressure instrumentation. Afterbody pressure orifices are shown for rows at ϕ = 30°, 90°, and bottom center line. Open symbols indicate orifices hidden from view. All dimensions are in inches.

Nozzle Configuration	Non-afterburning		Afterburning	
Exit variables	Config. I	Config. III	Configs. I and II	Config. IV
Shroud exit sta	76.000	79.000	76.000	79.000
d_e	3.985	4.001	3.985	4.001
d_j	2.858	2.833	3.763	3.780
d_t	-------	-------	3.340	3.401
δ	0.610	0.640	0.460	0.490
A_b/S	0.01461	0.01514	0.00324	0.00325

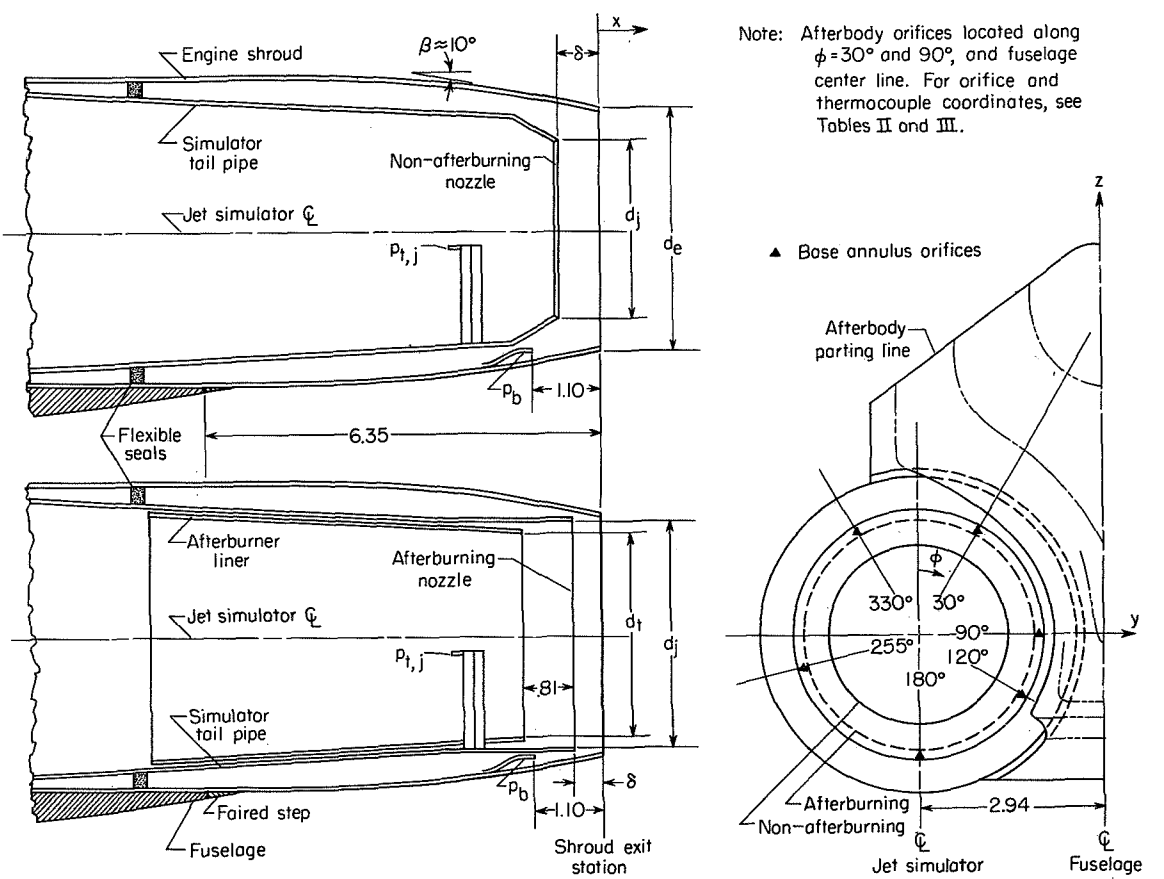

Figure 5.- Geometrical details of jet-exit configurations and angular position of base and afterbody instrumentation. Base areas are given for two engines. All dimensions are in inches unless otherwise noted.

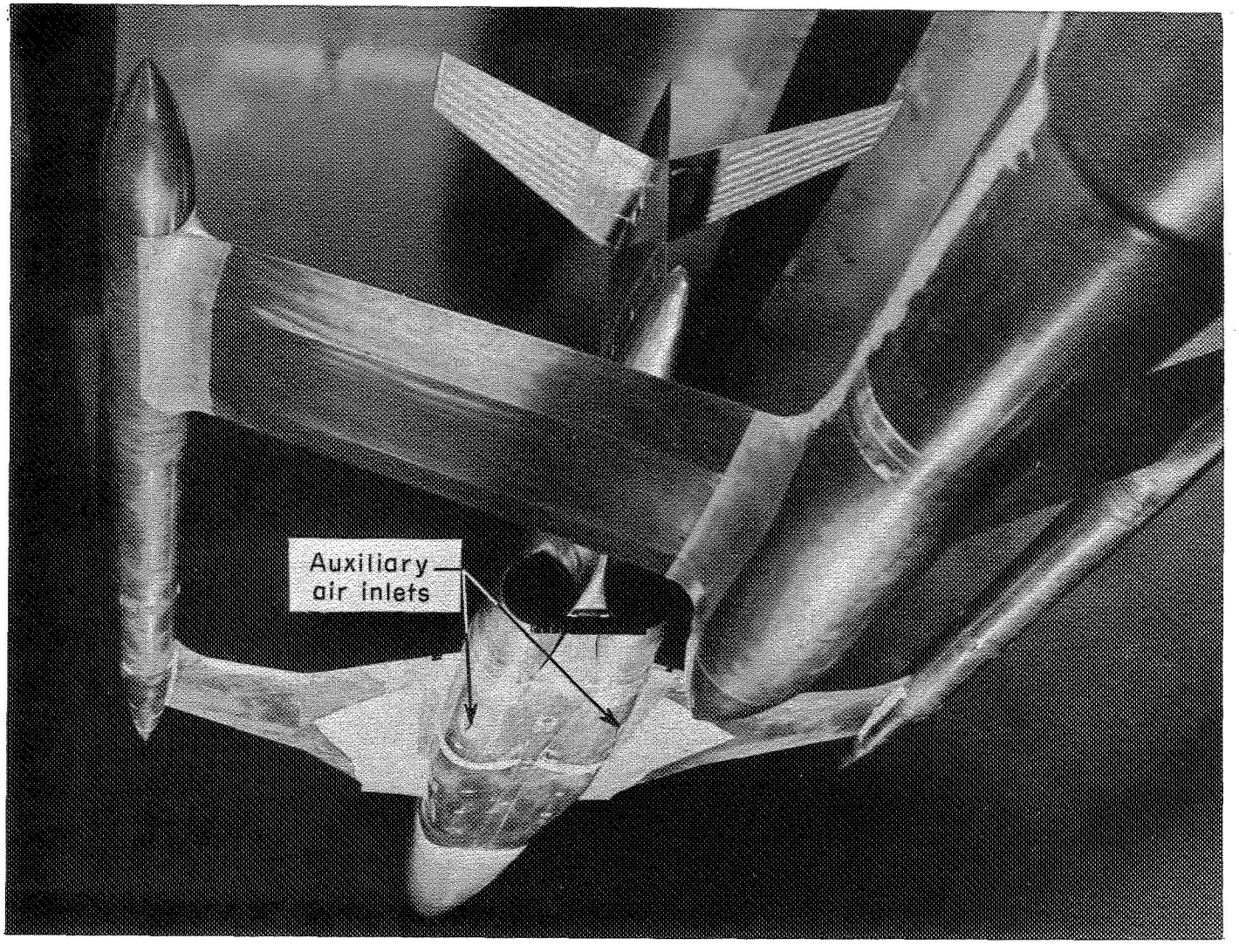

Figure 6.- Rear view of model showing auxiliary air inlets. L-93843

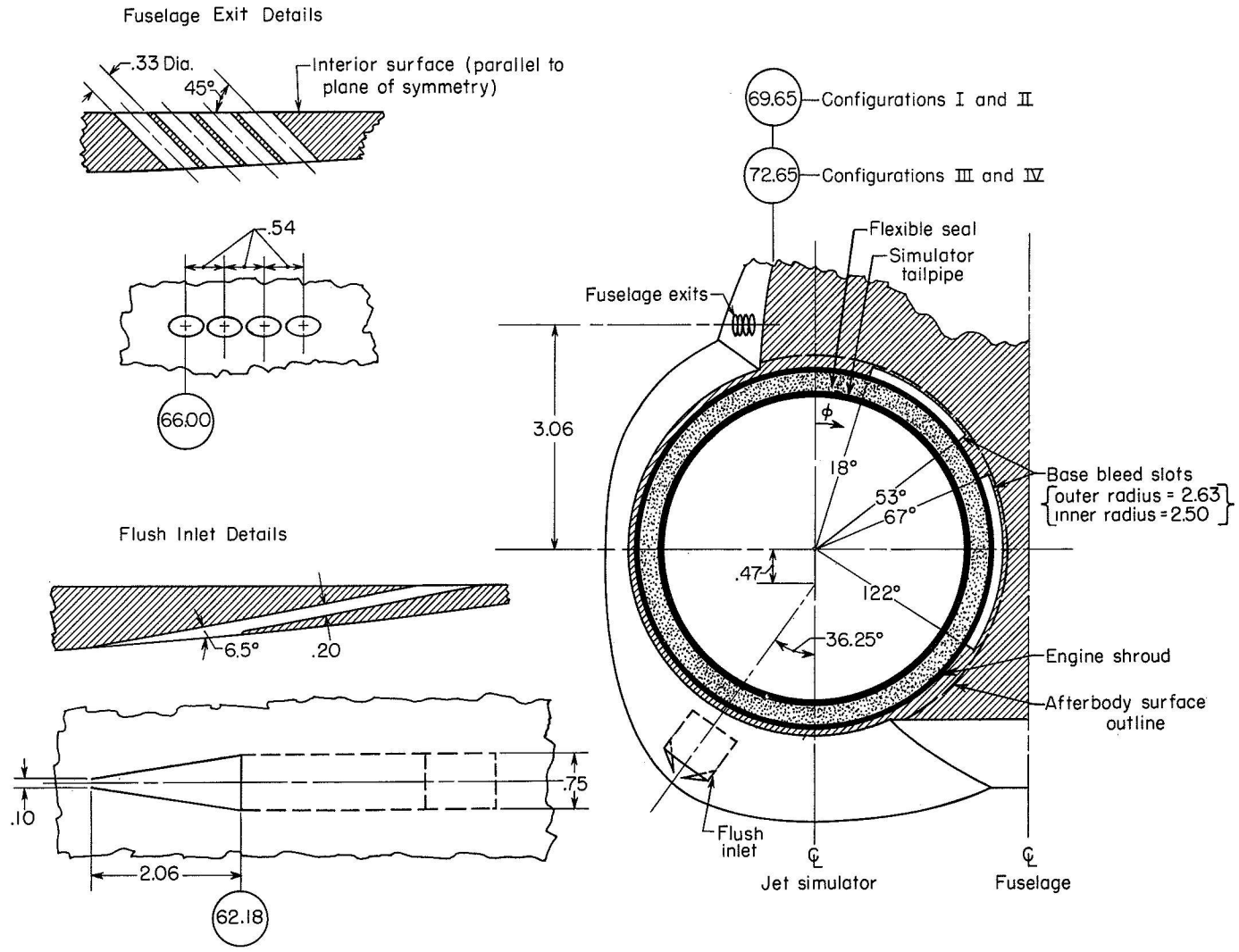

Figure 7.- Geometrical details of the auxiliary air system components. All dimensions are in inches unless otherwise noted.

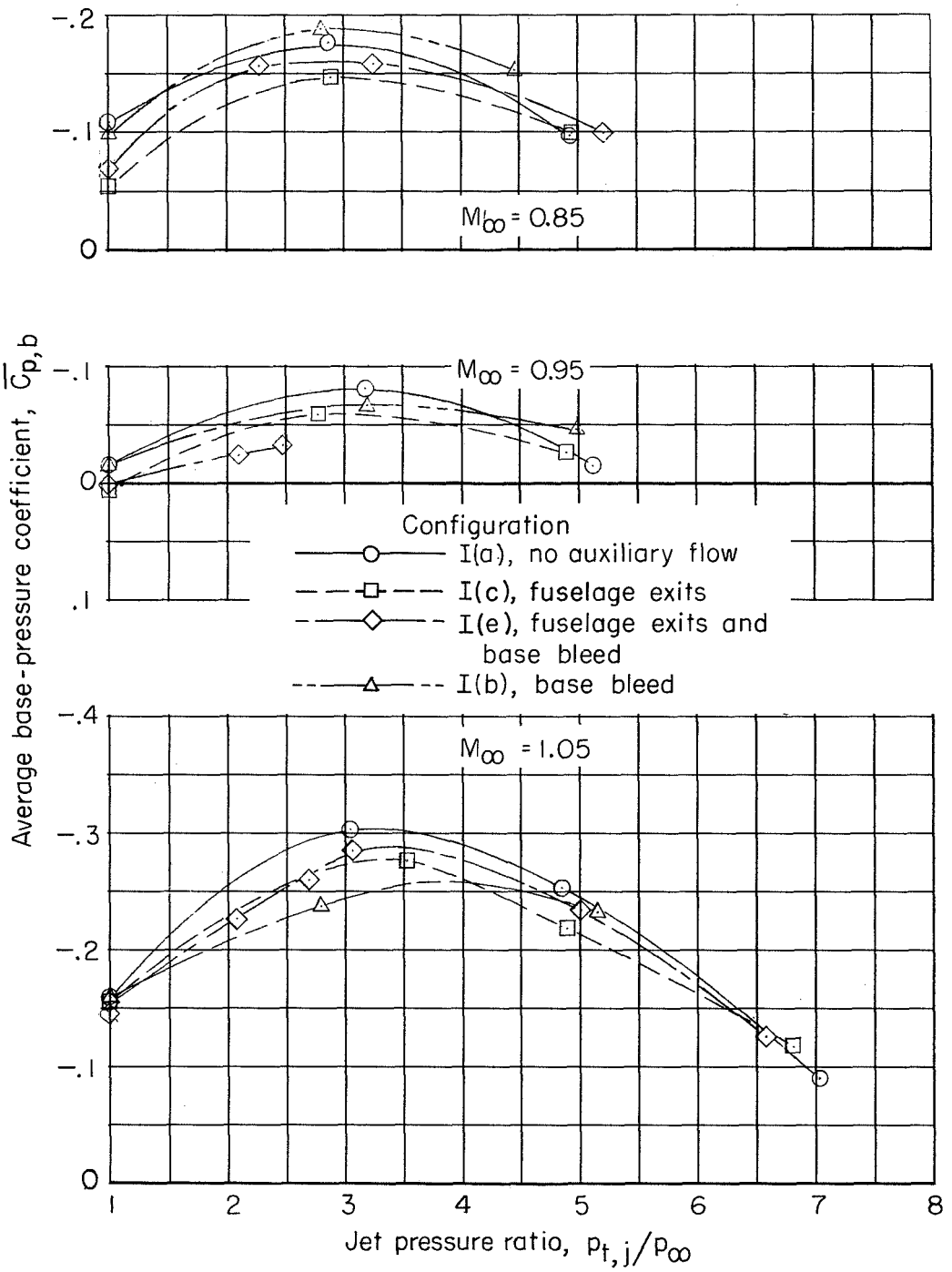

Figure 8.- Variation of average base-pressure coefficient with jet-pressure ratio for various types of auxiliary air flow. Configuration I; $\alpha = 4^\circ$.

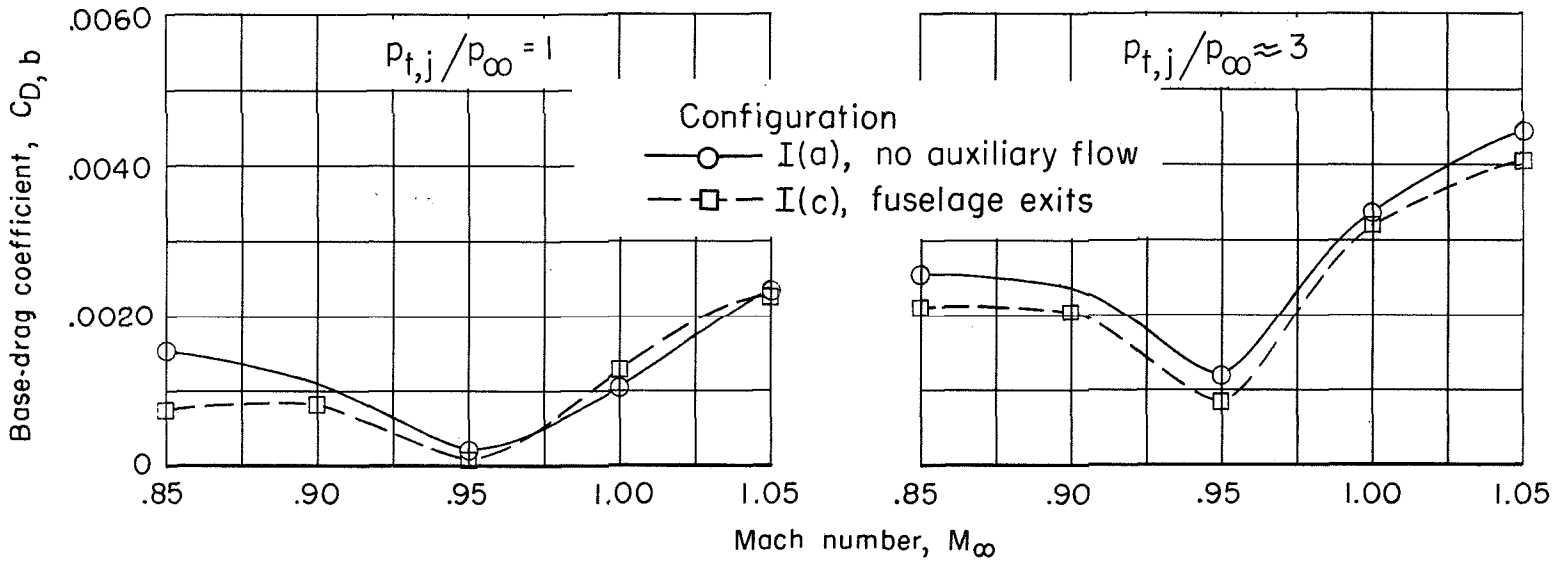

Figure 9.- Influence of auxiliary air flow on the variation of base-drag coefficient with Mach number. Configuration I; $\alpha = 4^{\circ}$.

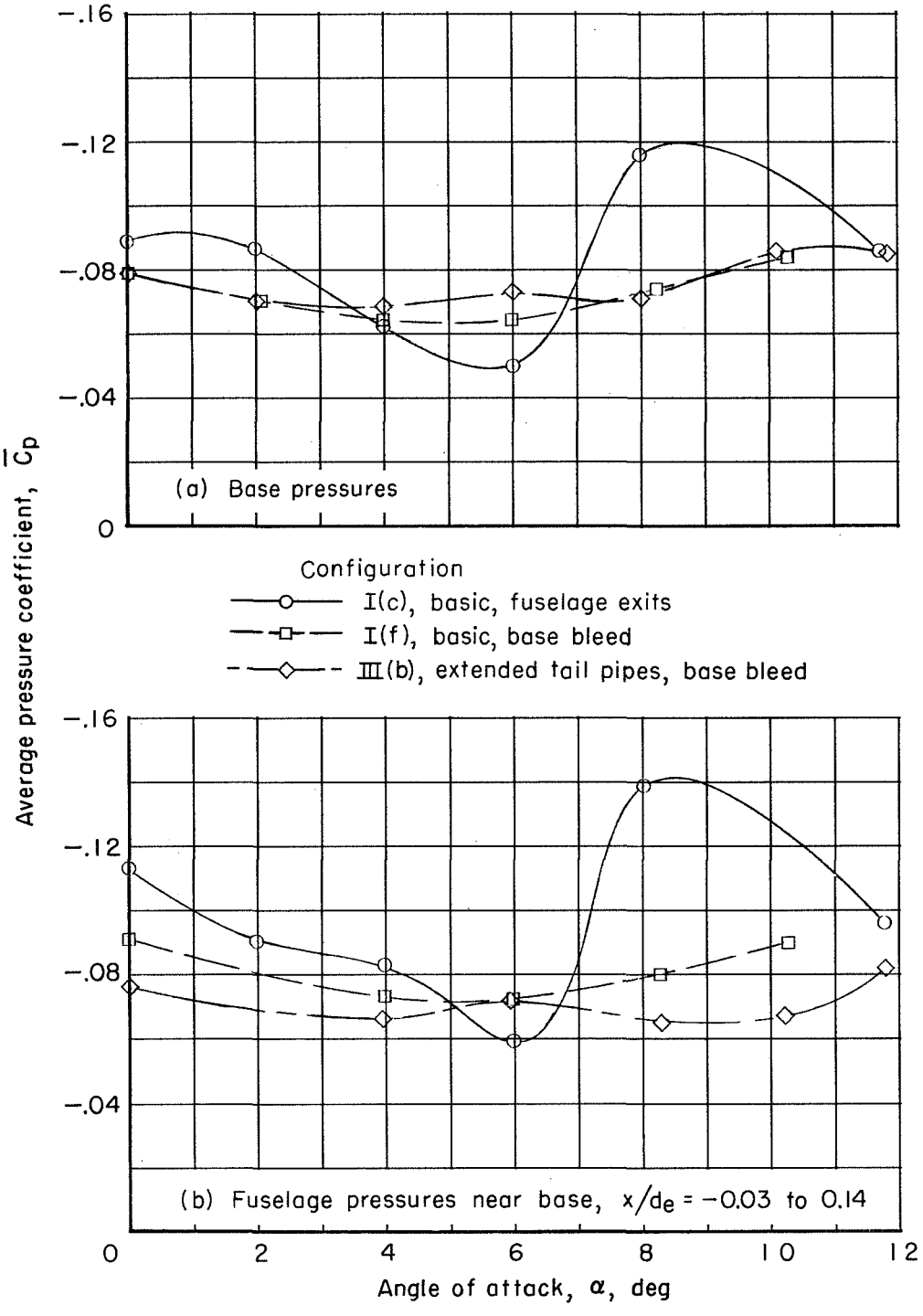

Figure 10.- Variation of average pressure coefficients in engine base region with angle of attack. $M_\infty = 0.85$, jets off.

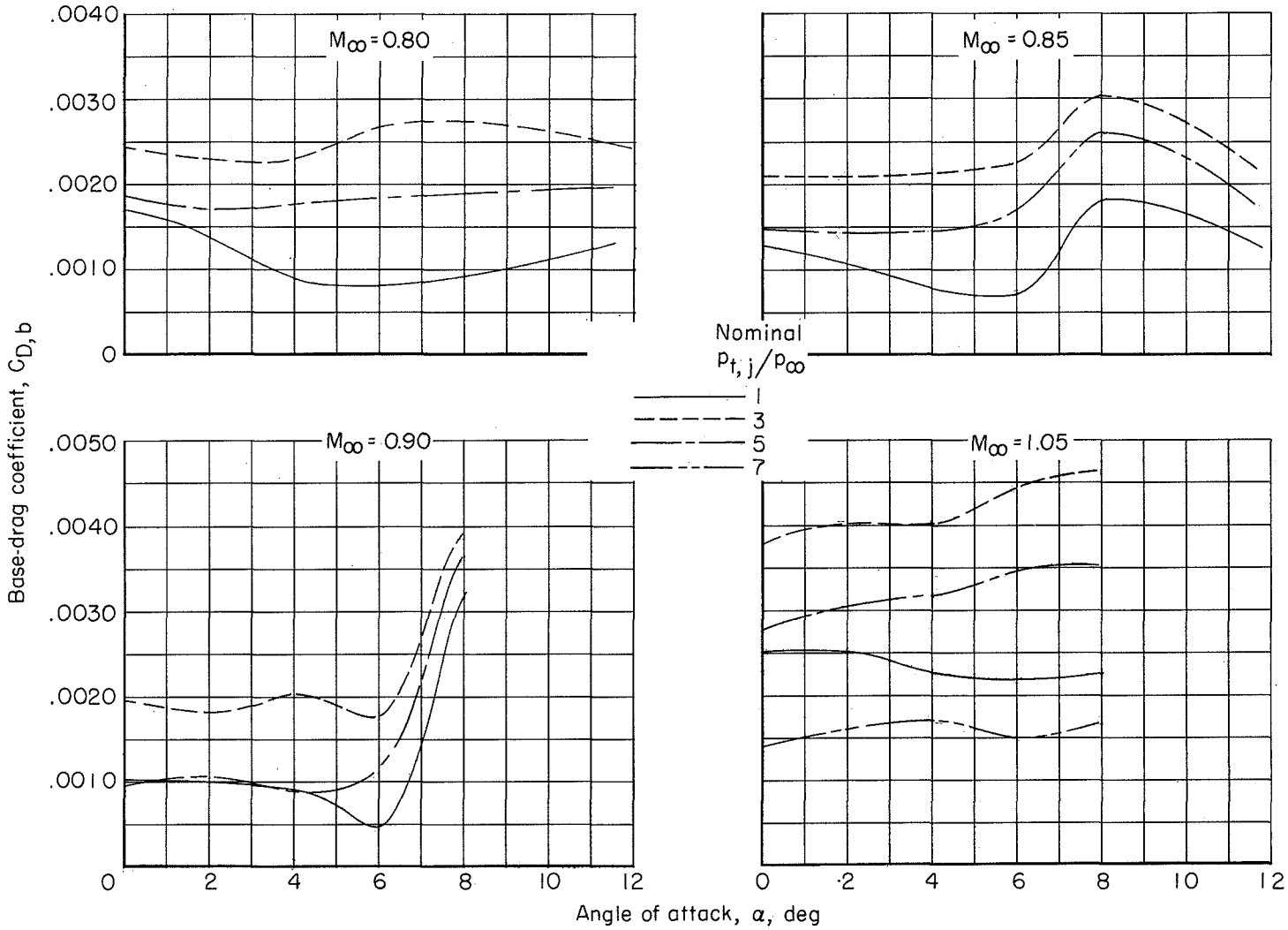

Figure 11.- Variation of base-drag coefficient with angle of attack for several pressure ratios. Configuration I(c); auxiliary air from fuselage exits.

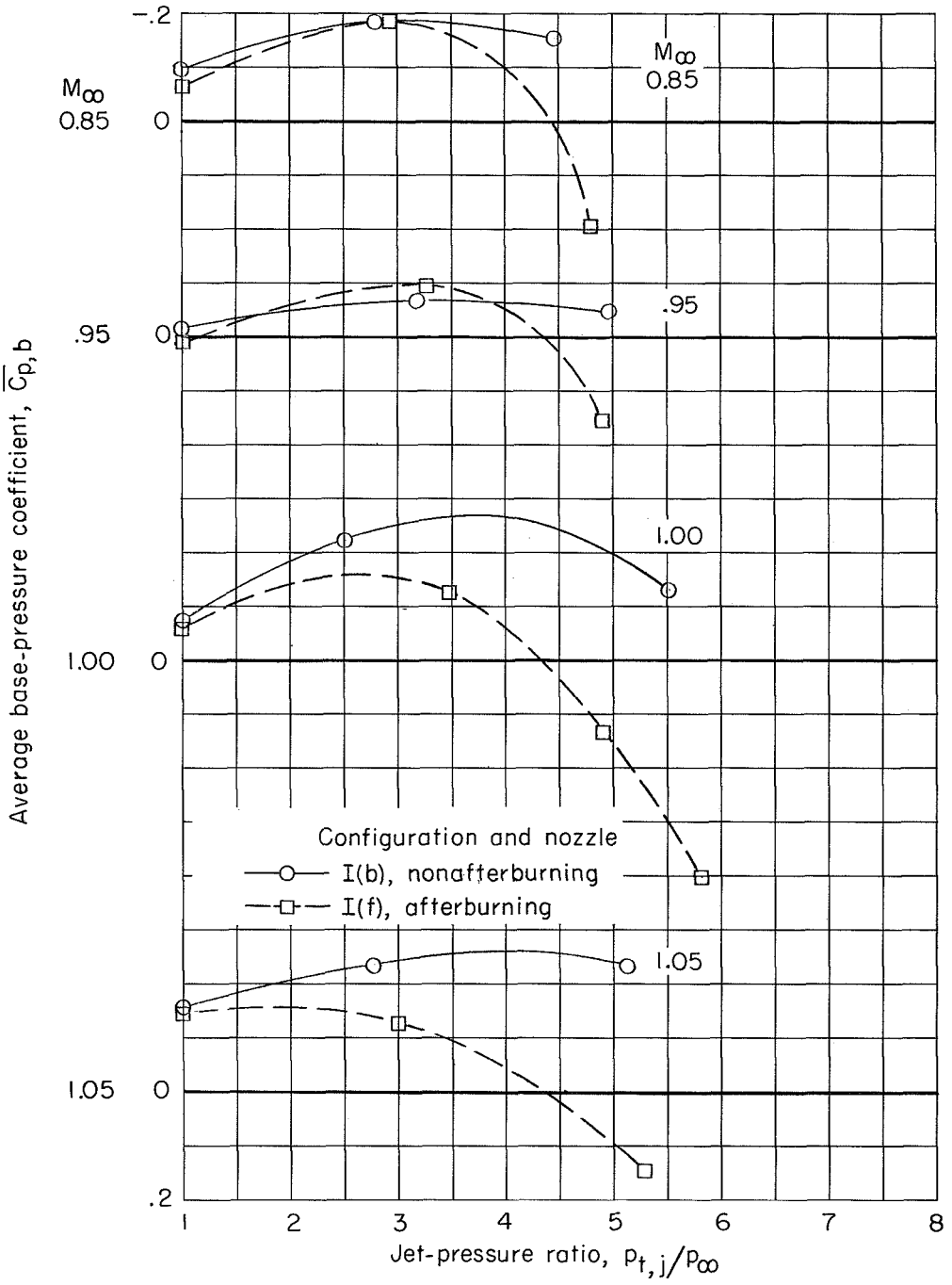

(a) Configurations I(b) and I(f).

Figure 12.- Effect of jet nozzle size on average base-pressure coefficients. $\alpha = 4^\circ$; auxiliary air from base bleed.

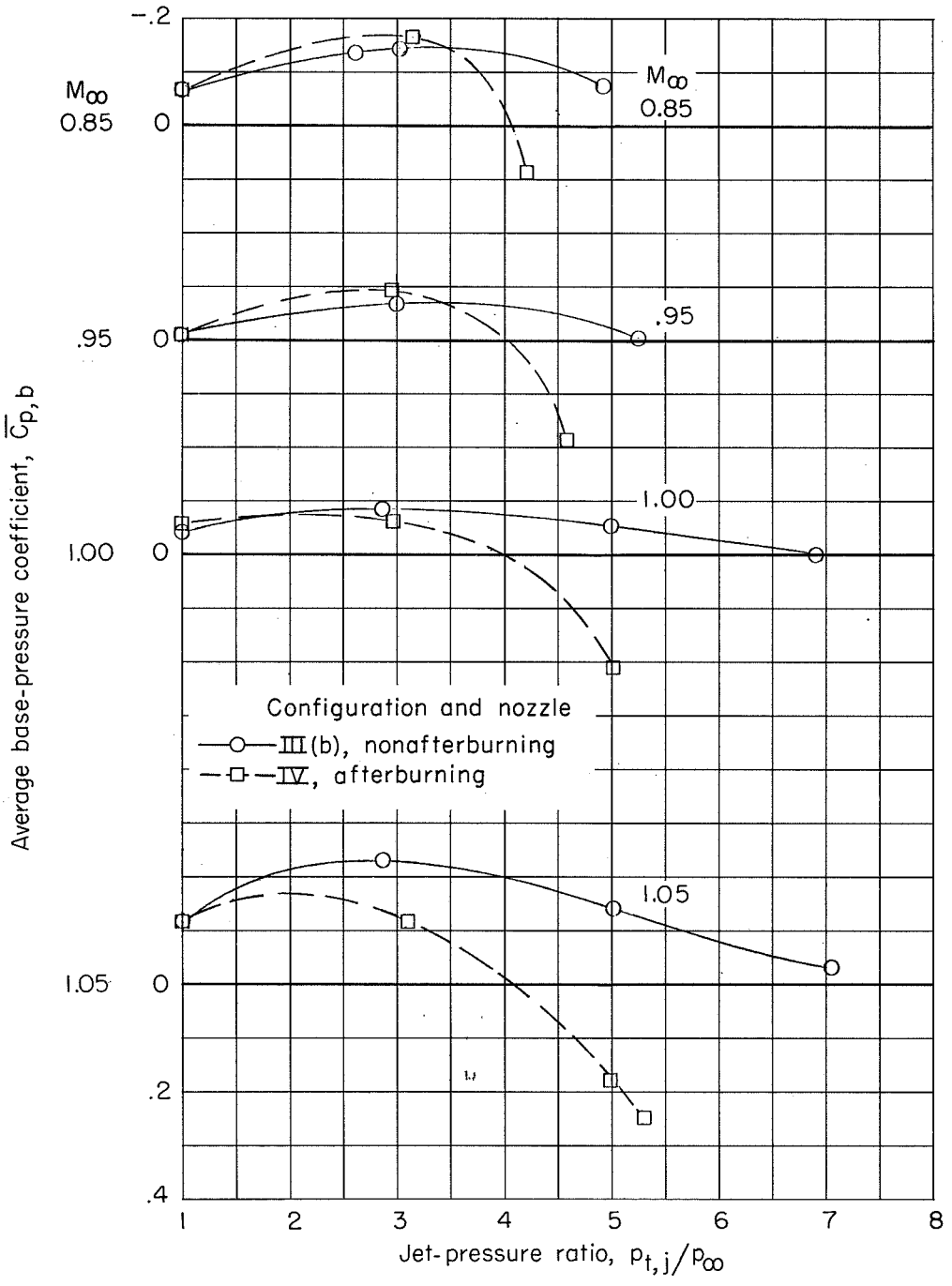

(b) Configurations III(b) and IV.

Figure 12.- Concluded.

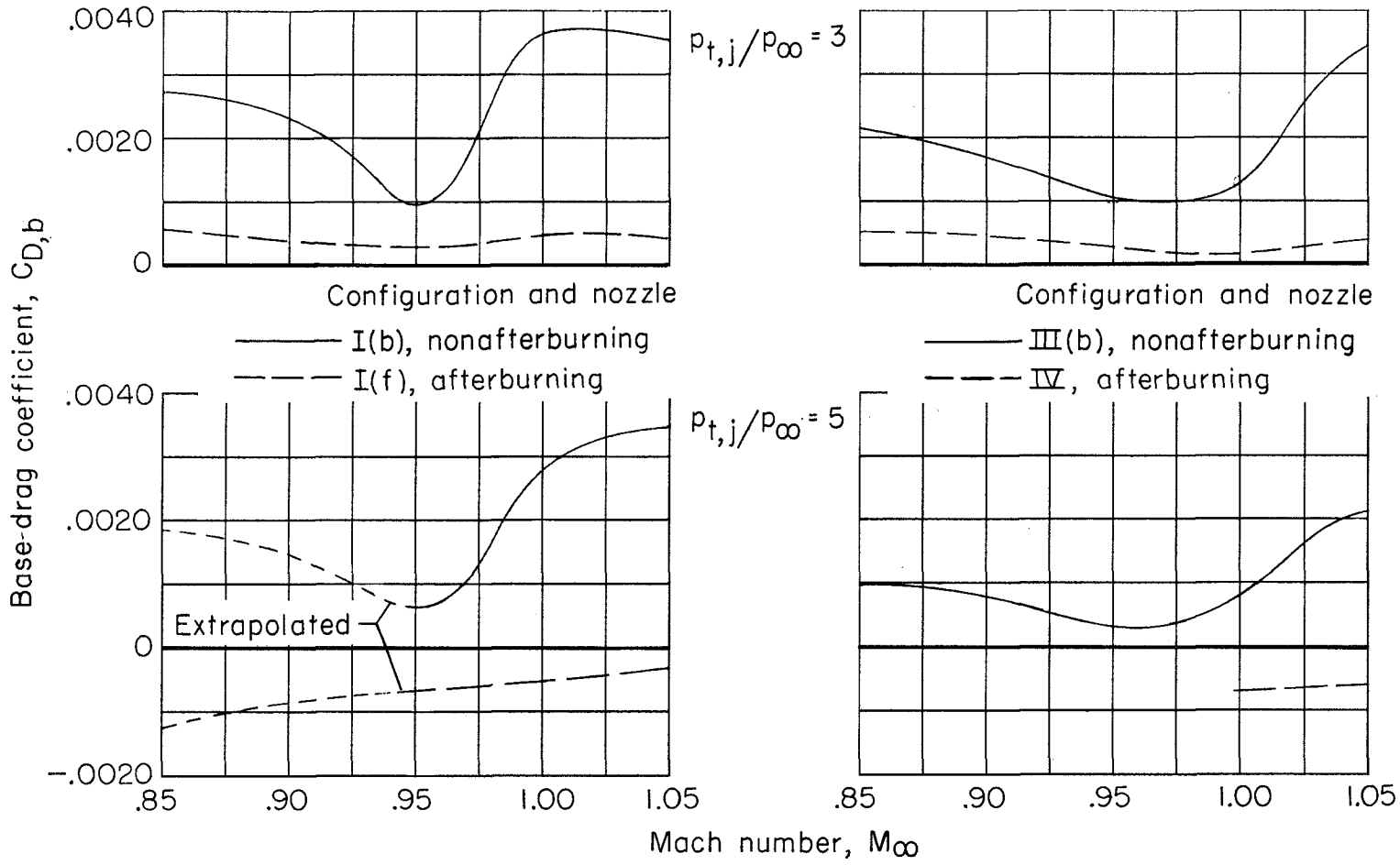

Figure 13.- Variation of base-drag coefficient with Mach number for nonafterburning and afterburning nozzles. Configurations I, III, and IV; $\alpha = 4^{\circ}$; auxiliary air from fuselage exits.

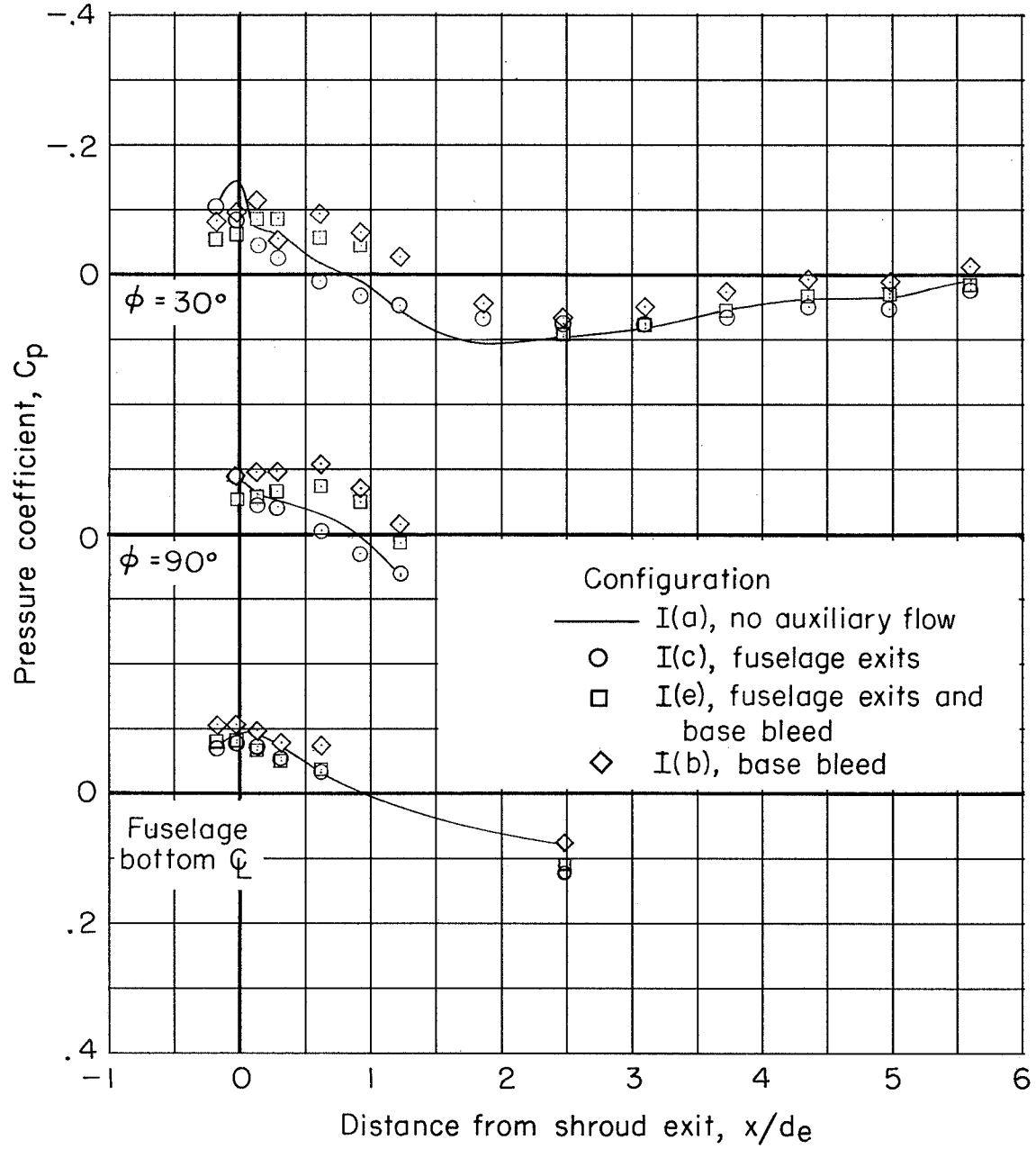

(a) $p_{t,j}/p_\infty = 1.$

Figure 14.- Typical effect of auxiliary air flow on afterbody pressure distributions. Configuration I; $M_\infty = 0.85$; and $\alpha = 4^\circ$.

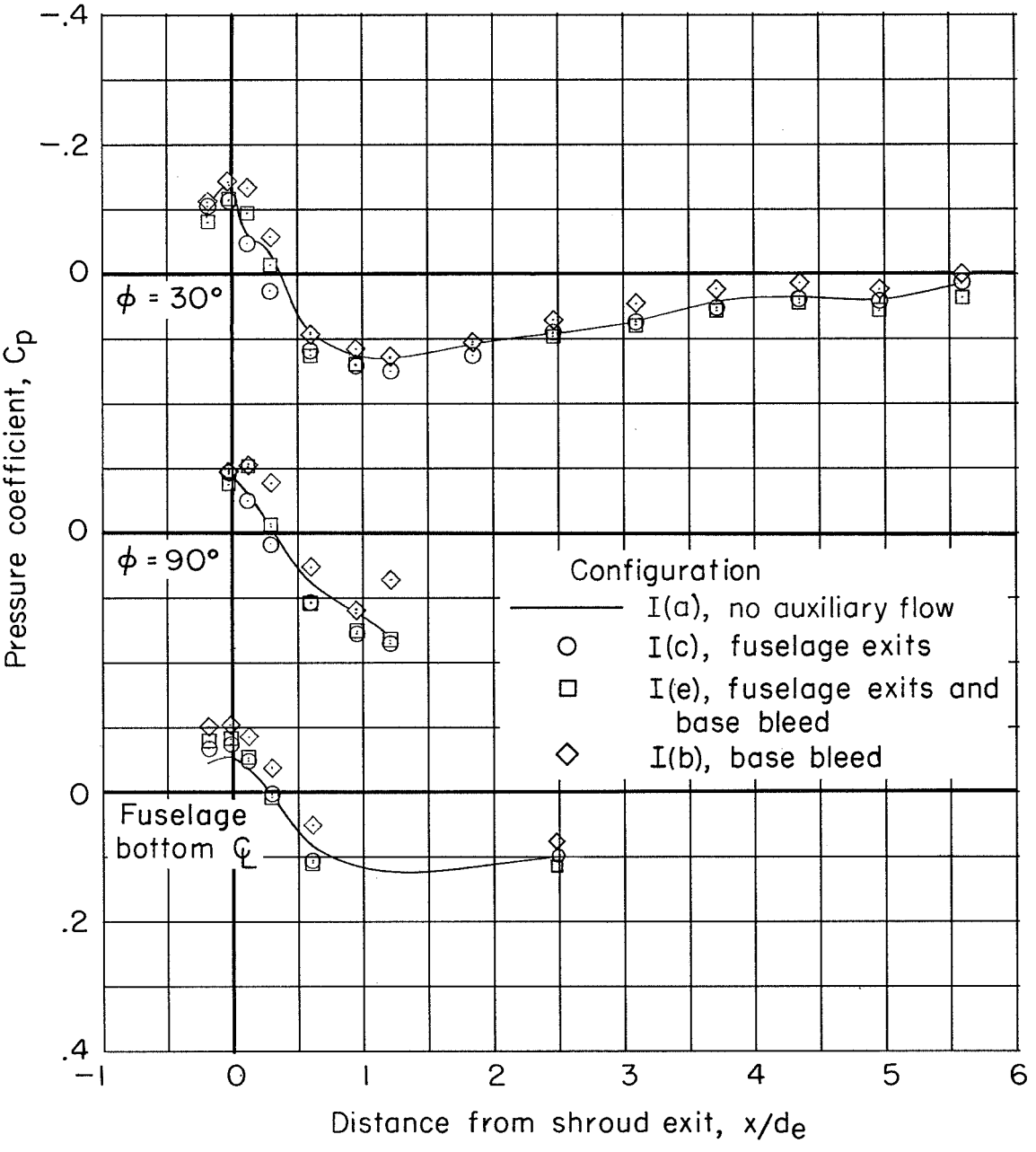

(b) $p_{t,j}/p_\infty = 3.$

Figure 14.- Concluded.

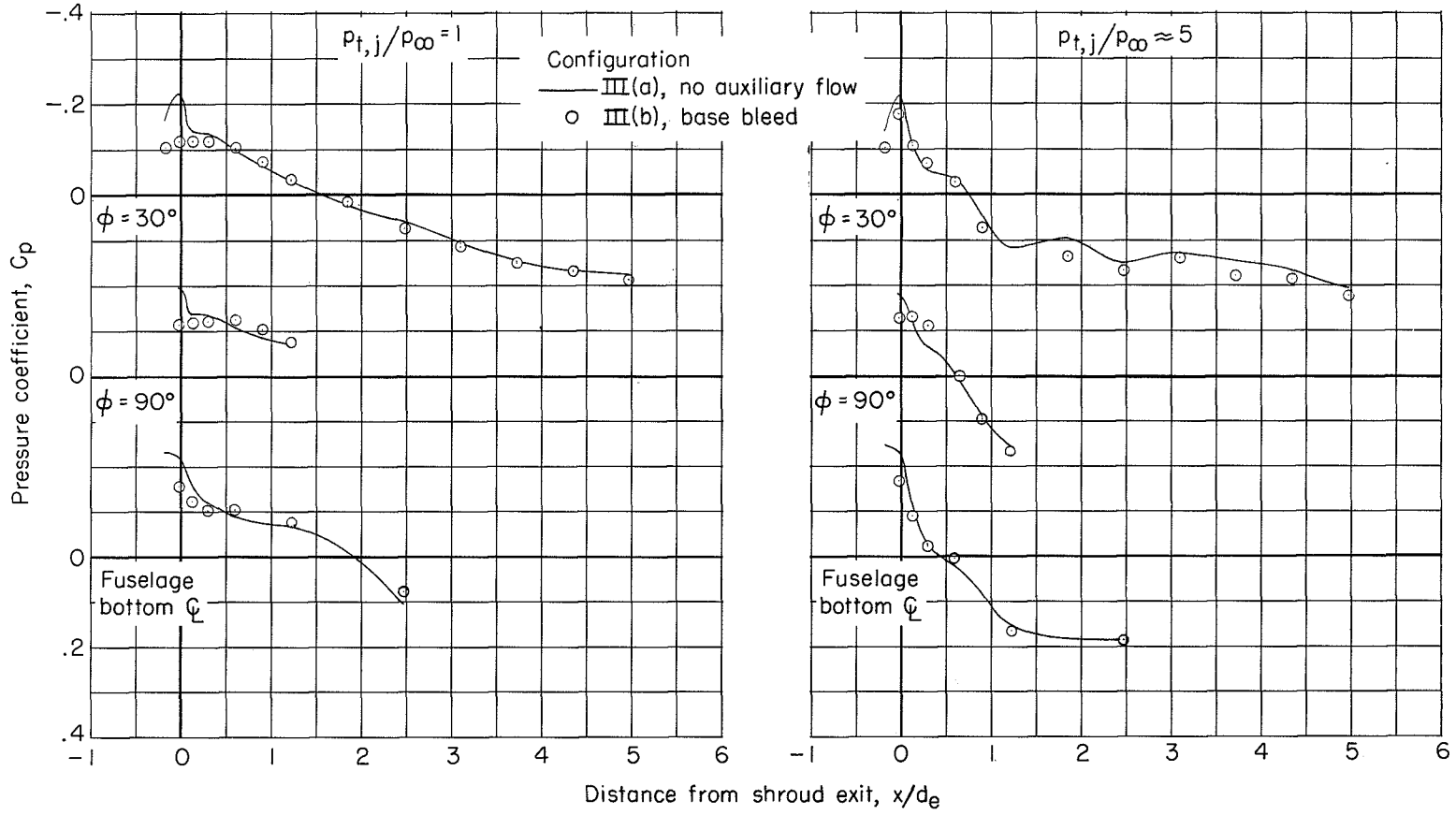

Figure 15.- Effect of base bleed on afterbody pressure distributions. Configuration III; $M_\infty = 1.05$; $\alpha = 4°$.

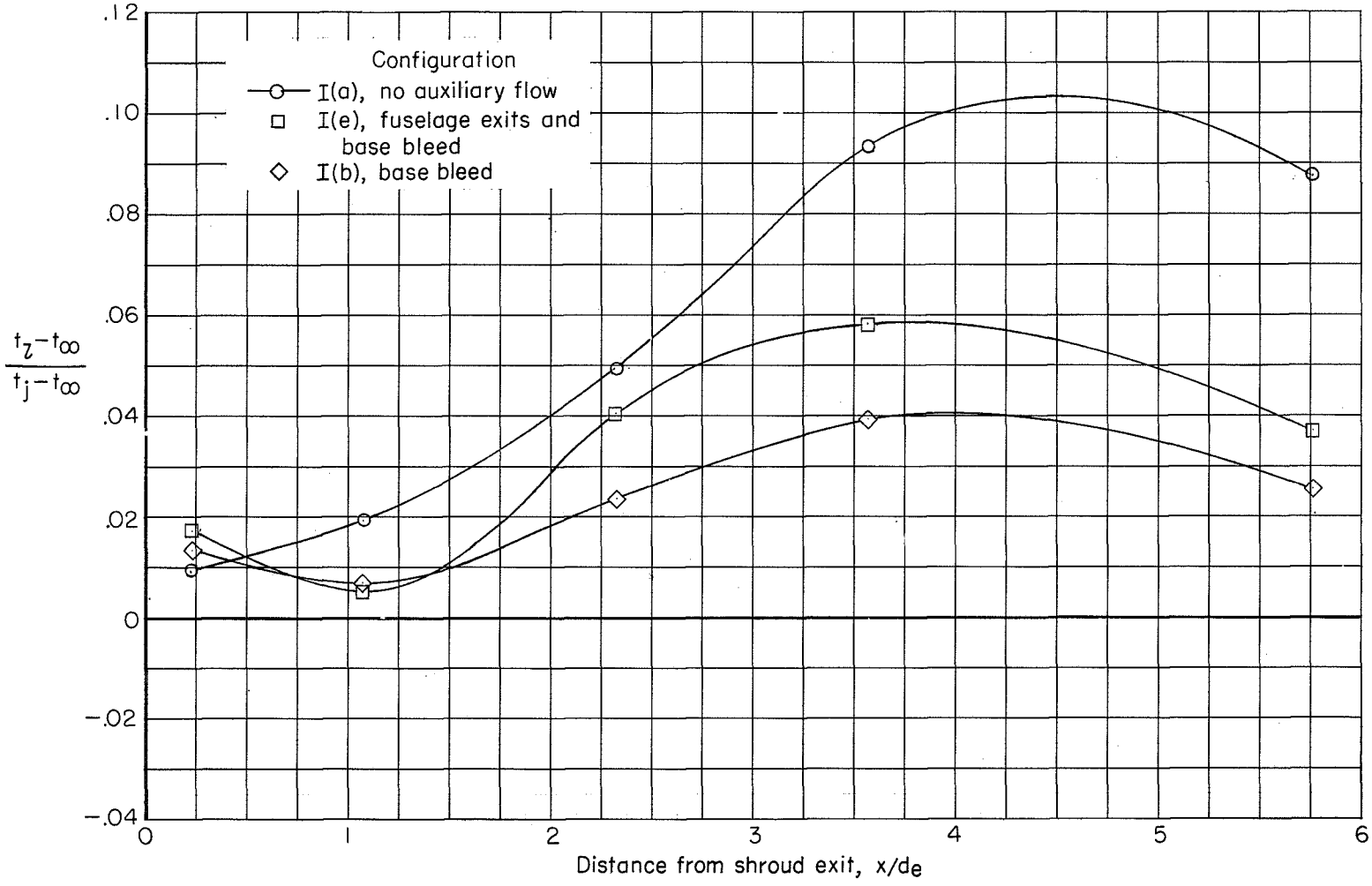

Figure 16.- Effect of auxiliary air flow on afterbody temperatures at $\phi = 30^\circ$. Configuration I; $M_\infty = 0.85$; $\alpha = 4^\circ$; and $p_{t,j}/p_\infty = 2.7$.

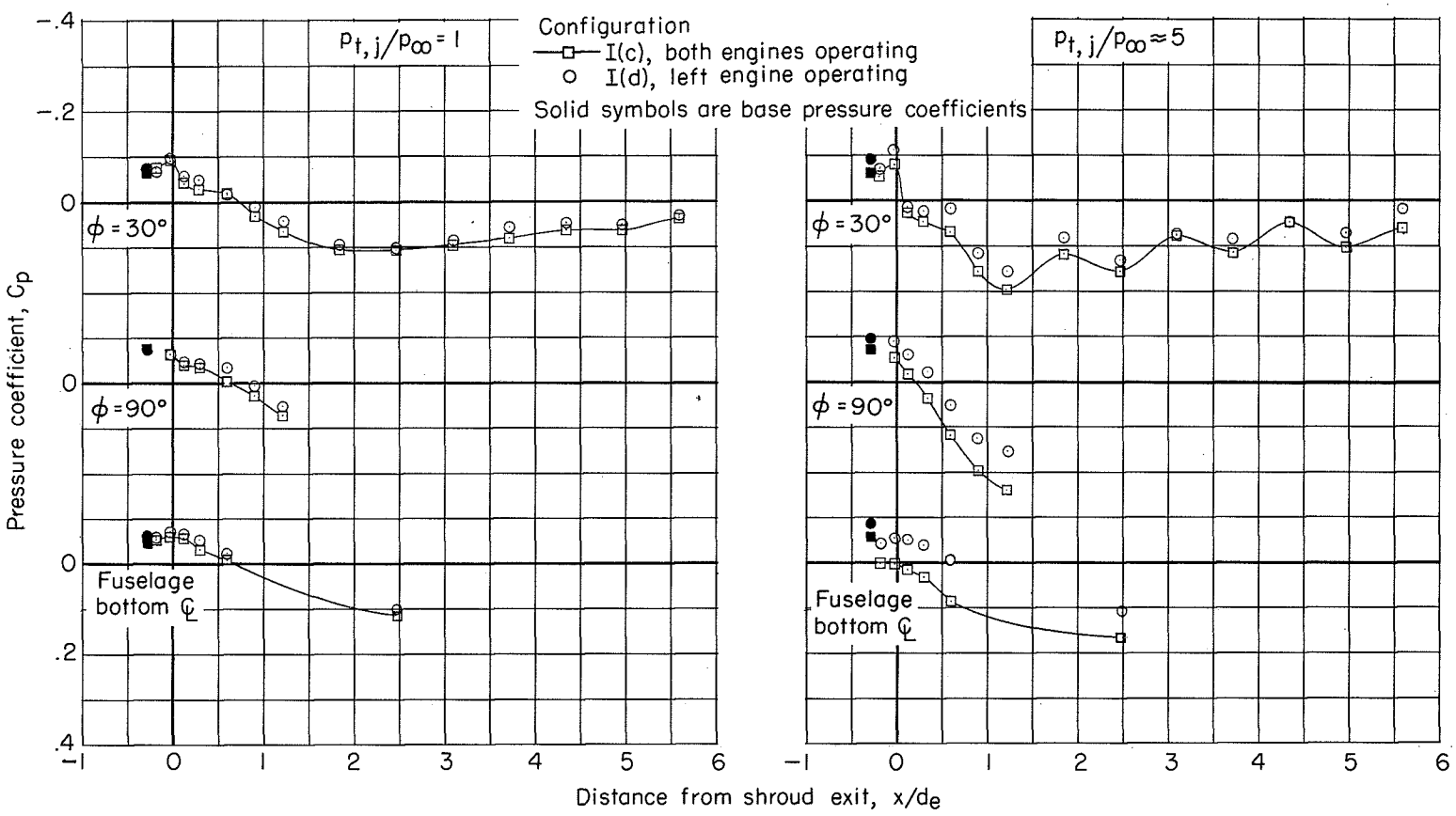

Figure 17.- Effect of single-engine operation on afterbody pressure distributions. Configuration I; $M_{\infty} = 0.90$; $\alpha = 4^{\circ}$; auxiliary air from fuselage exits.

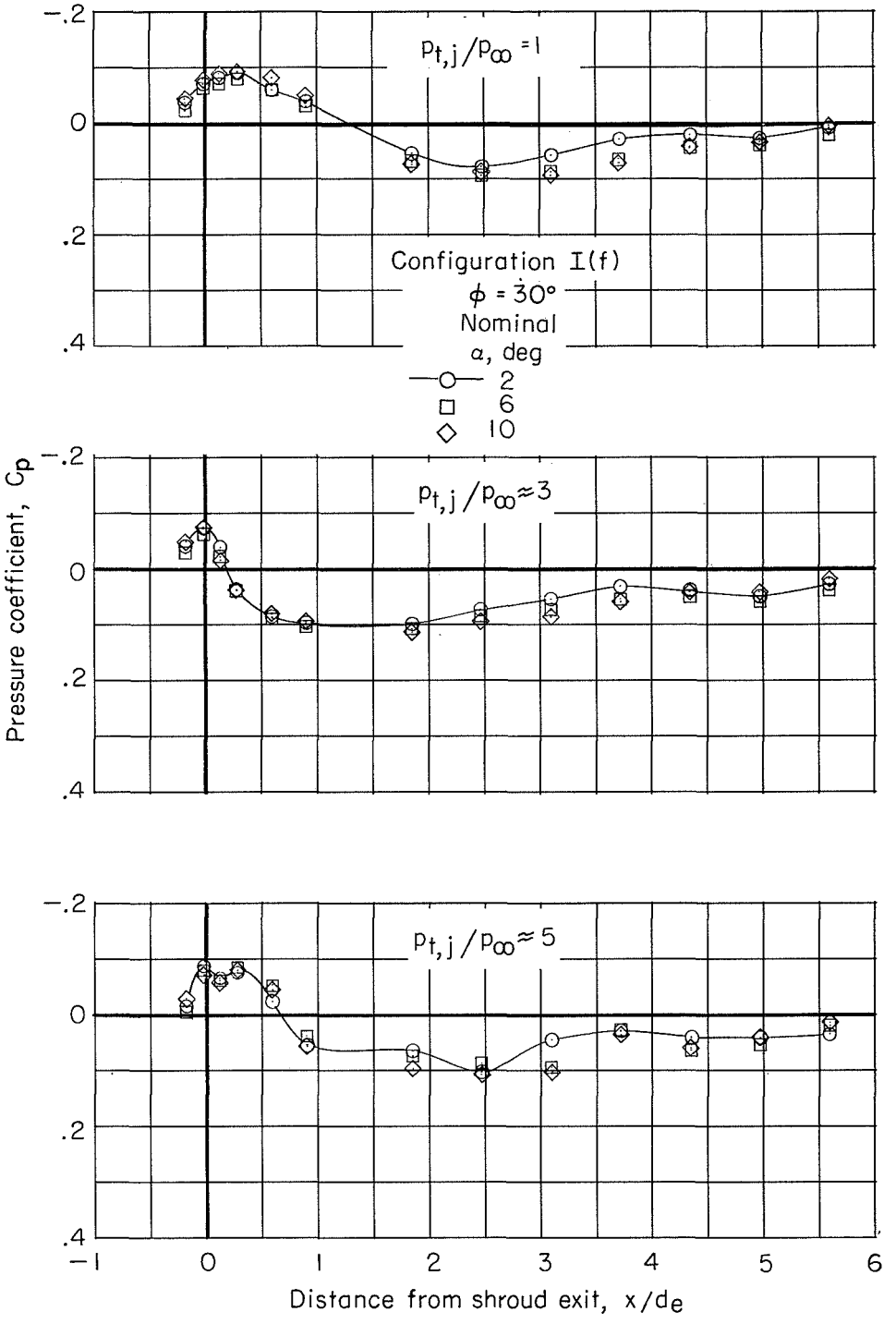

Figure 18.- Effect of angle of attack on afterbody pressure distributions. Configuration I(f); $M_\infty = 0.85$.

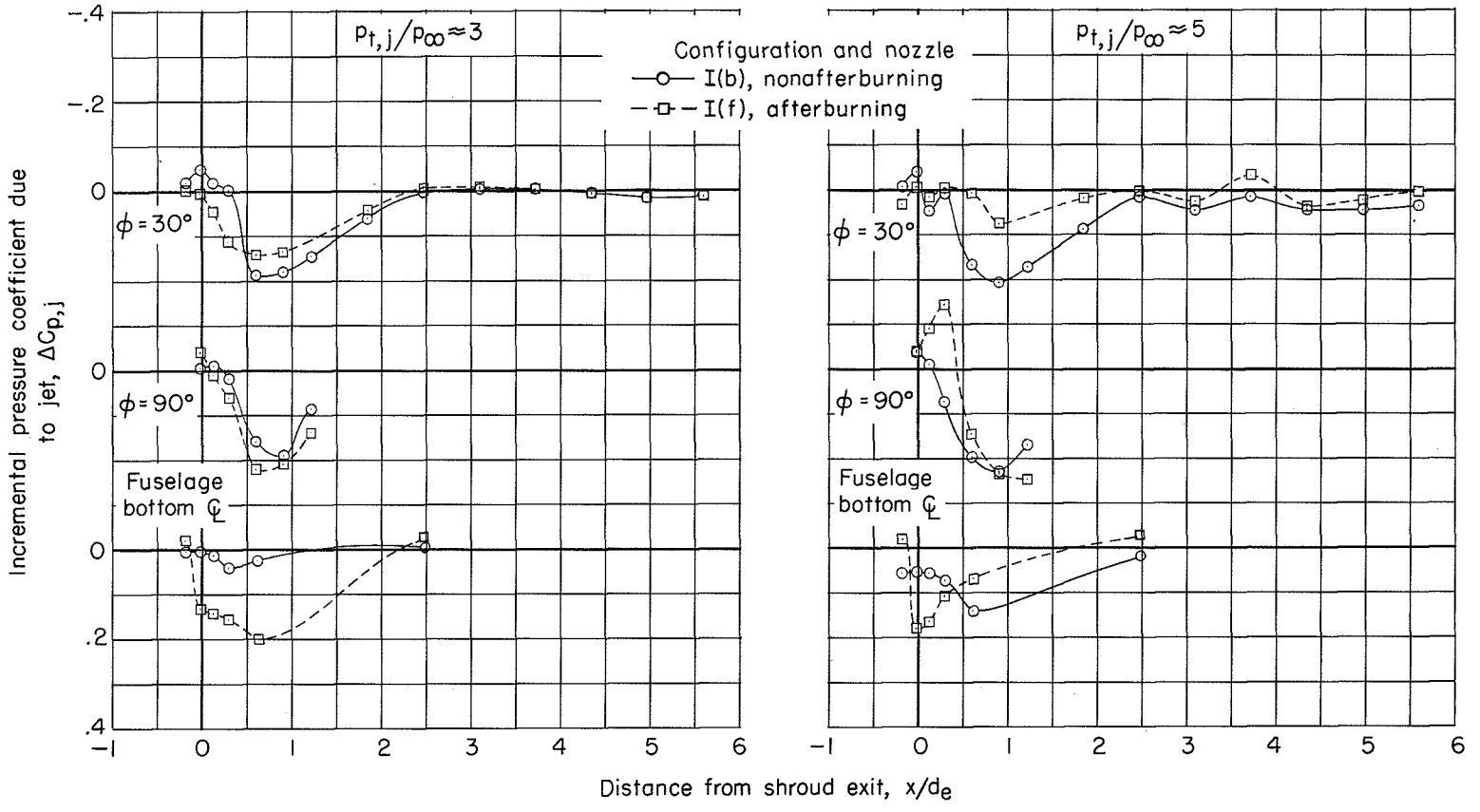

(a) $M_\infty = 0.85$.

Figure 19.- Afterbody incremental pressure coefficient due to jet operation with nonafterburning and afterburning nozzles. Configuration I; $\alpha = 4^\circ$; auxiliary air from base bleed.

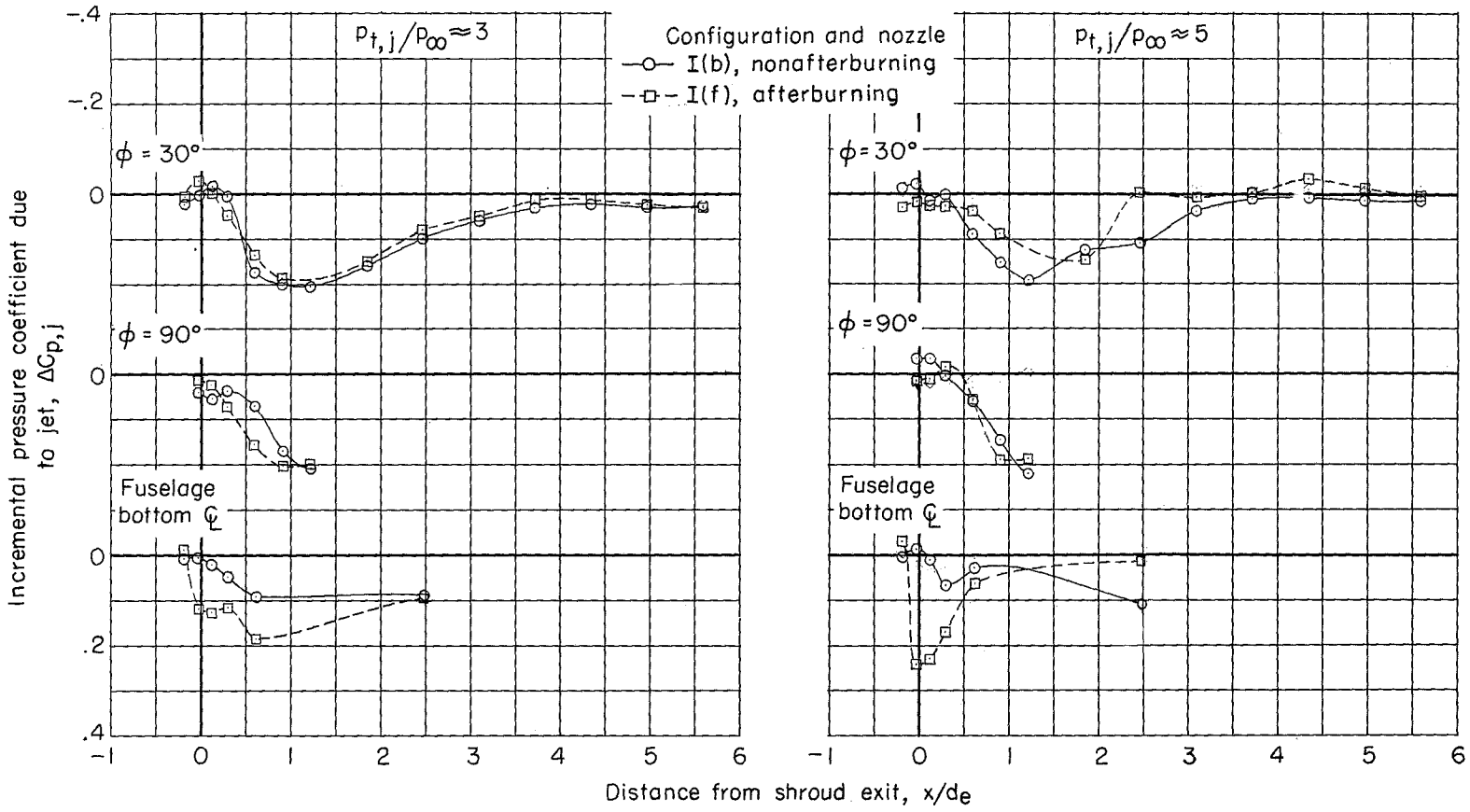

(b) $M_\infty = 1.05$.

Figure 19.- Concluded.

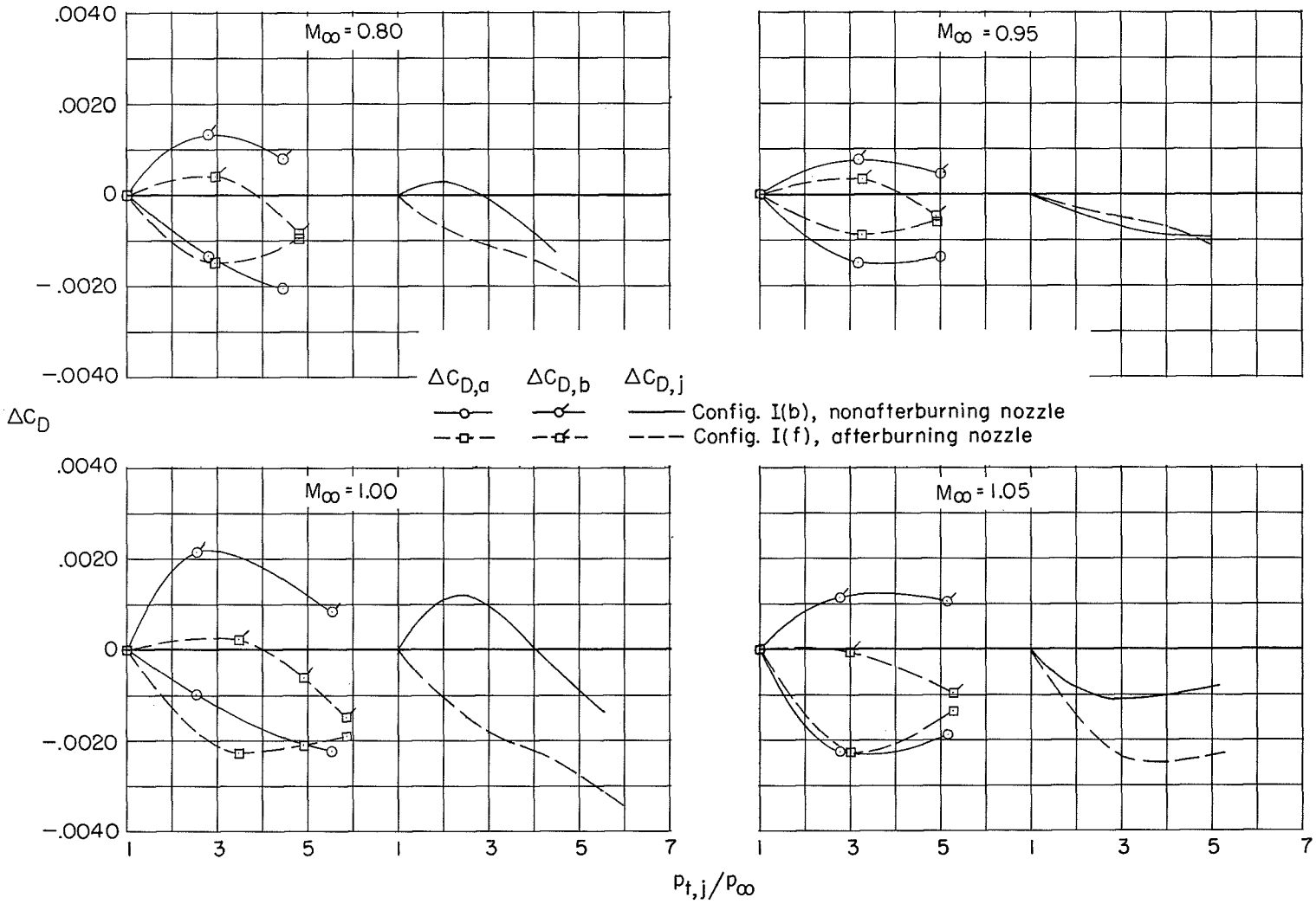

Figure 20.- Effect of jet operation on base and afterbody drag for the nonafterburning and afterburning nozzle configurations. $\alpha = 4^\circ$; auxiliary air from base bleed.

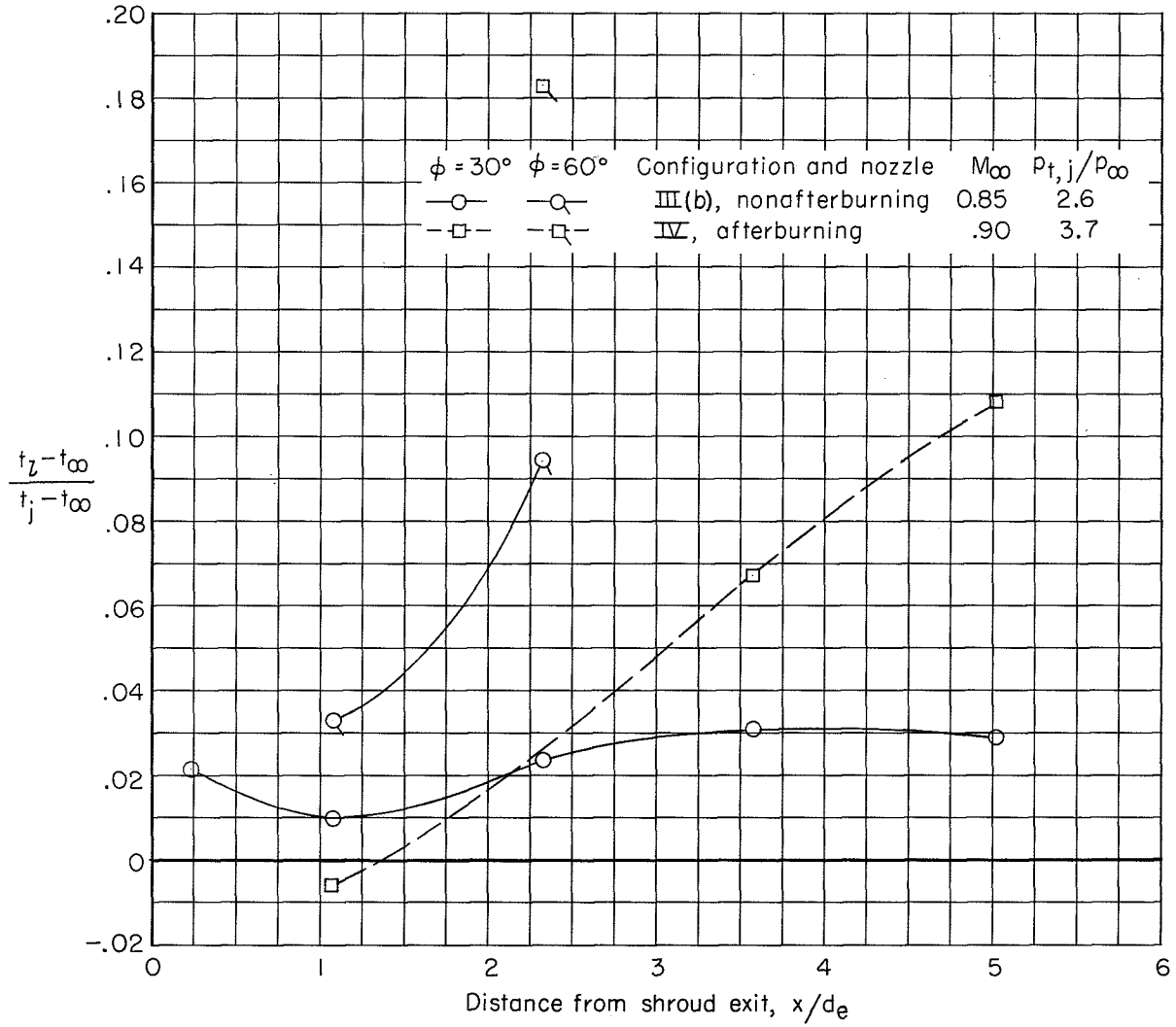

Figure 21.- Effect of nozzle configuration on afterbody temperatures at $\phi = 30°$ and $60°$. Configuration III (high tail) and configuration IV (low tail); $\alpha = 4°$.

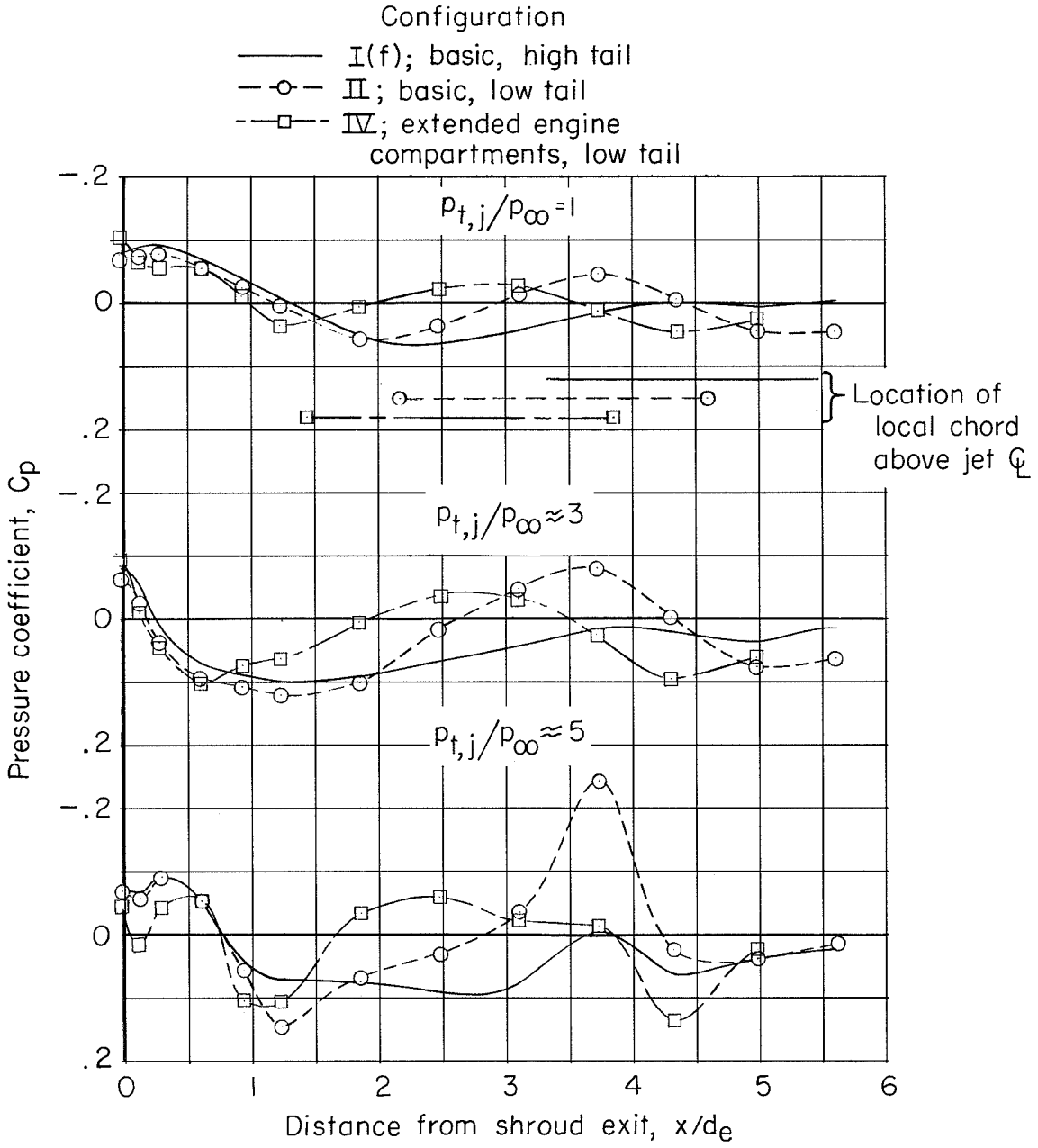

Figure 22.- Influence of horizontal-tail location on afterbody pressure distributions at $\phi = 30^\circ$. Configurations I(f), II, and IV; afterburning nozzles; $M_\infty = 0.85$; $\alpha = 4^\circ$.

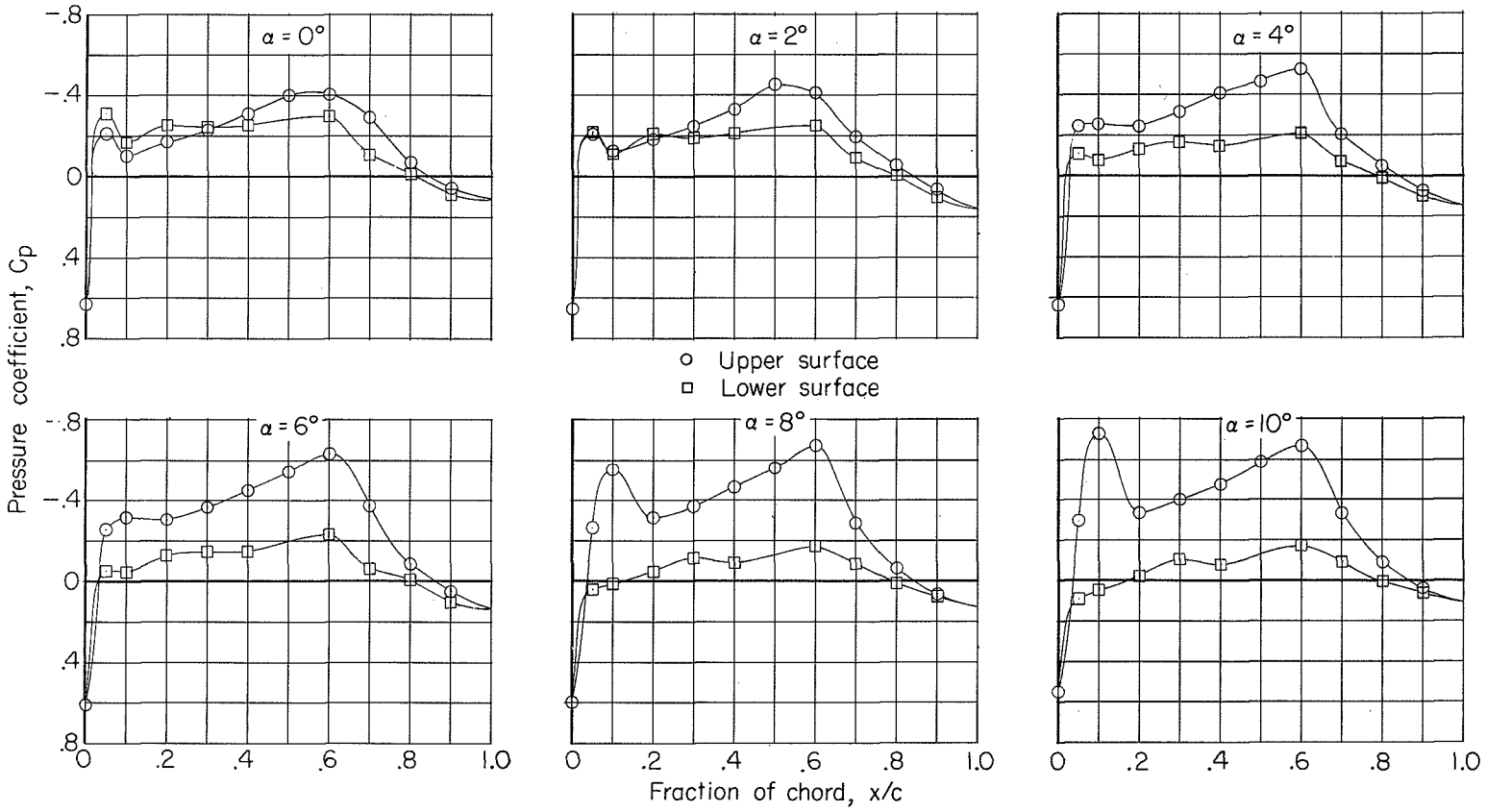

(a) Configuration I(f); high horizontal tail; $i_t = 0^\circ$.

Figure 23.- Pressure distributions on horizontal tail at various angles of attack. Jets off; $M_\infty = 0.85$.

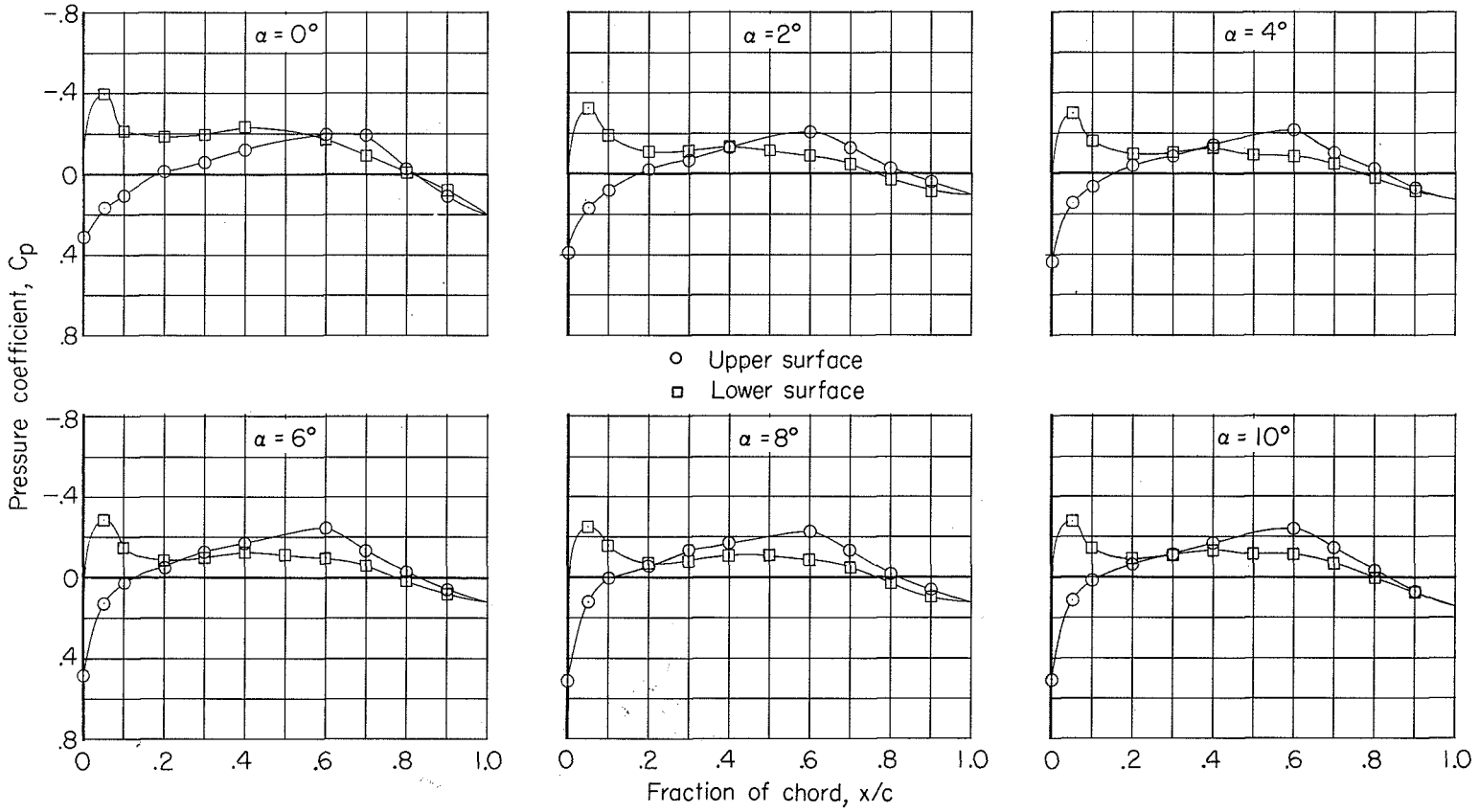

(b) Configuration II; low horizontal tail; $i_t = -2.6°$.

Figure 23.- Continued.

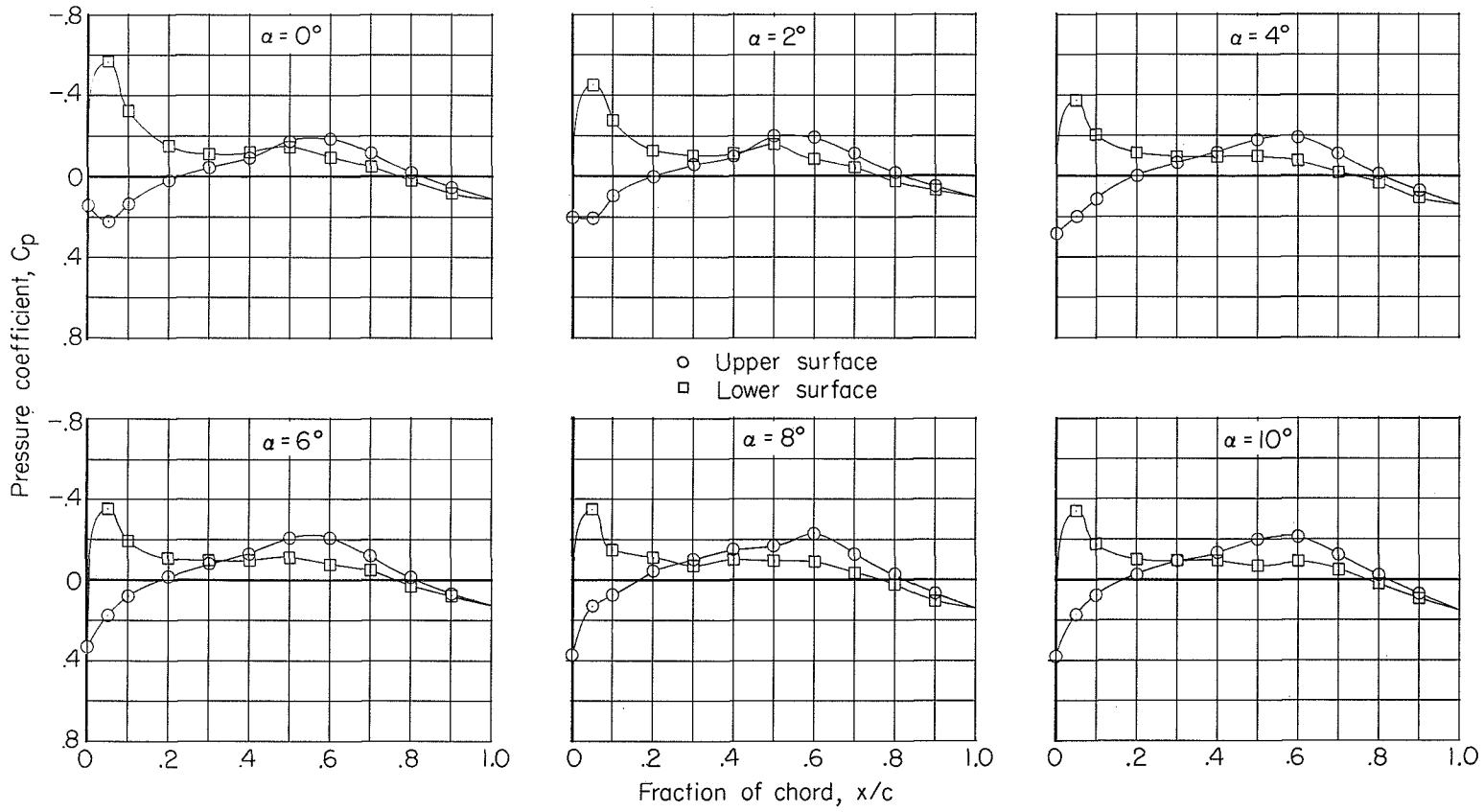

(c) Configuration IV; low horizontal tail; $i_t = -2.6^\circ$.

Figure 23.- Concluded.

Figure 24.- Effect of Mach number on horizontal-tail pressure distributions. Configurations I and II; jets off; $\alpha = 4^\circ$.

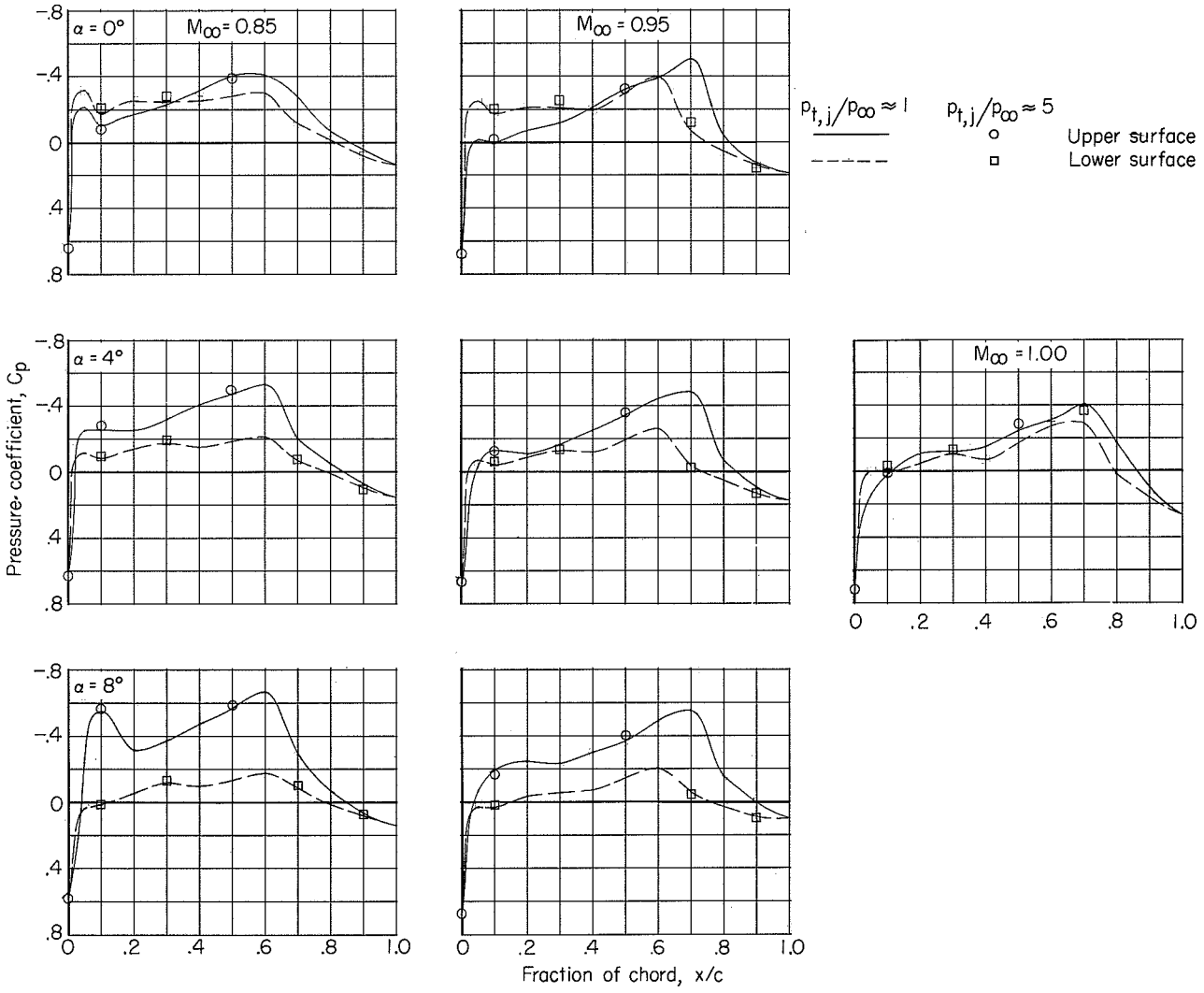

Figure 25.- Effect of jet operation on horizontal-tail pressure distribution. Configuration I(f); high horizontal tail.

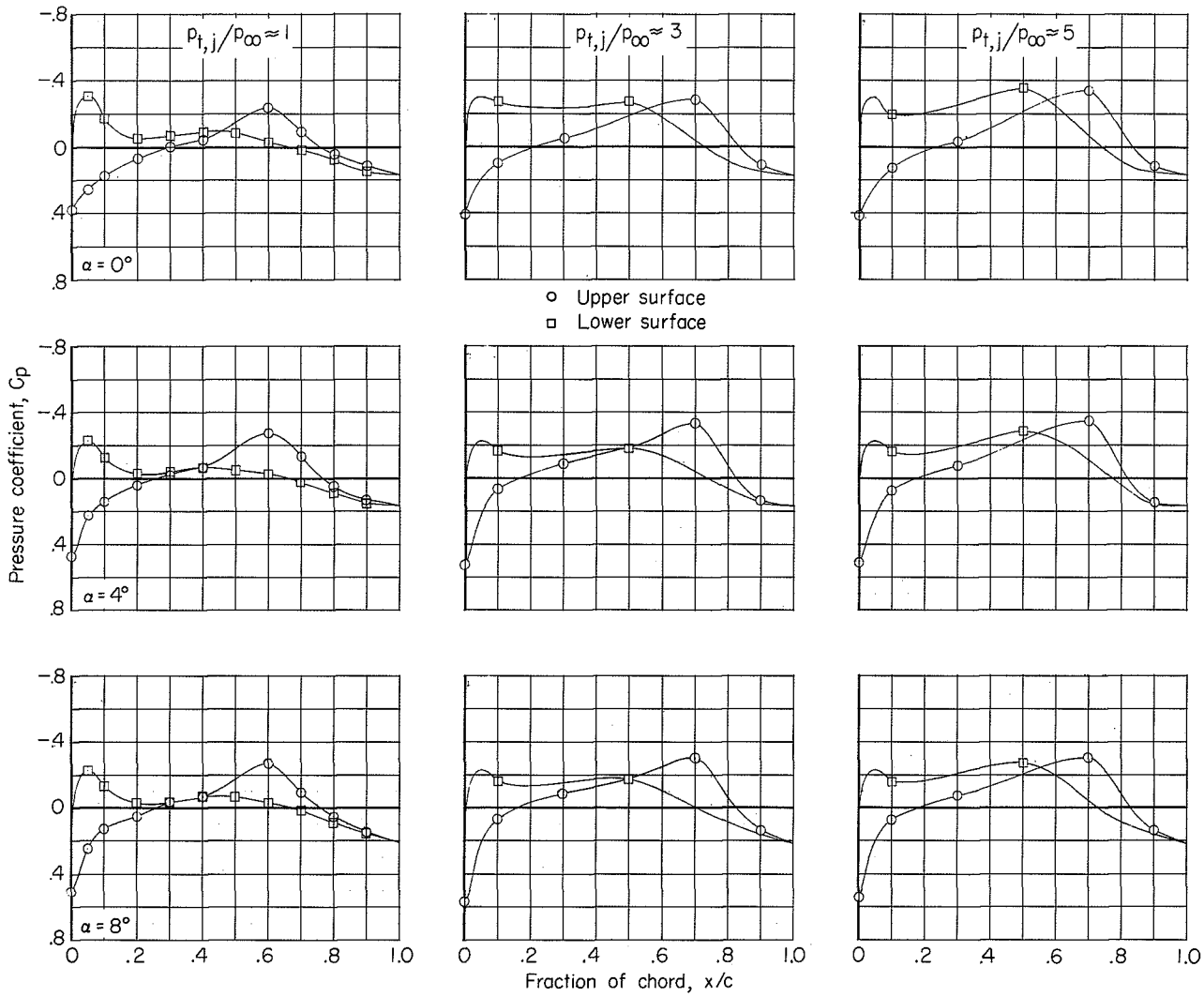

Figure 26.- Effect of jet operation on horizontal-tail pressure distribution. Configuration II; low horizontal tail; $M_{\infty} = 0.95$.

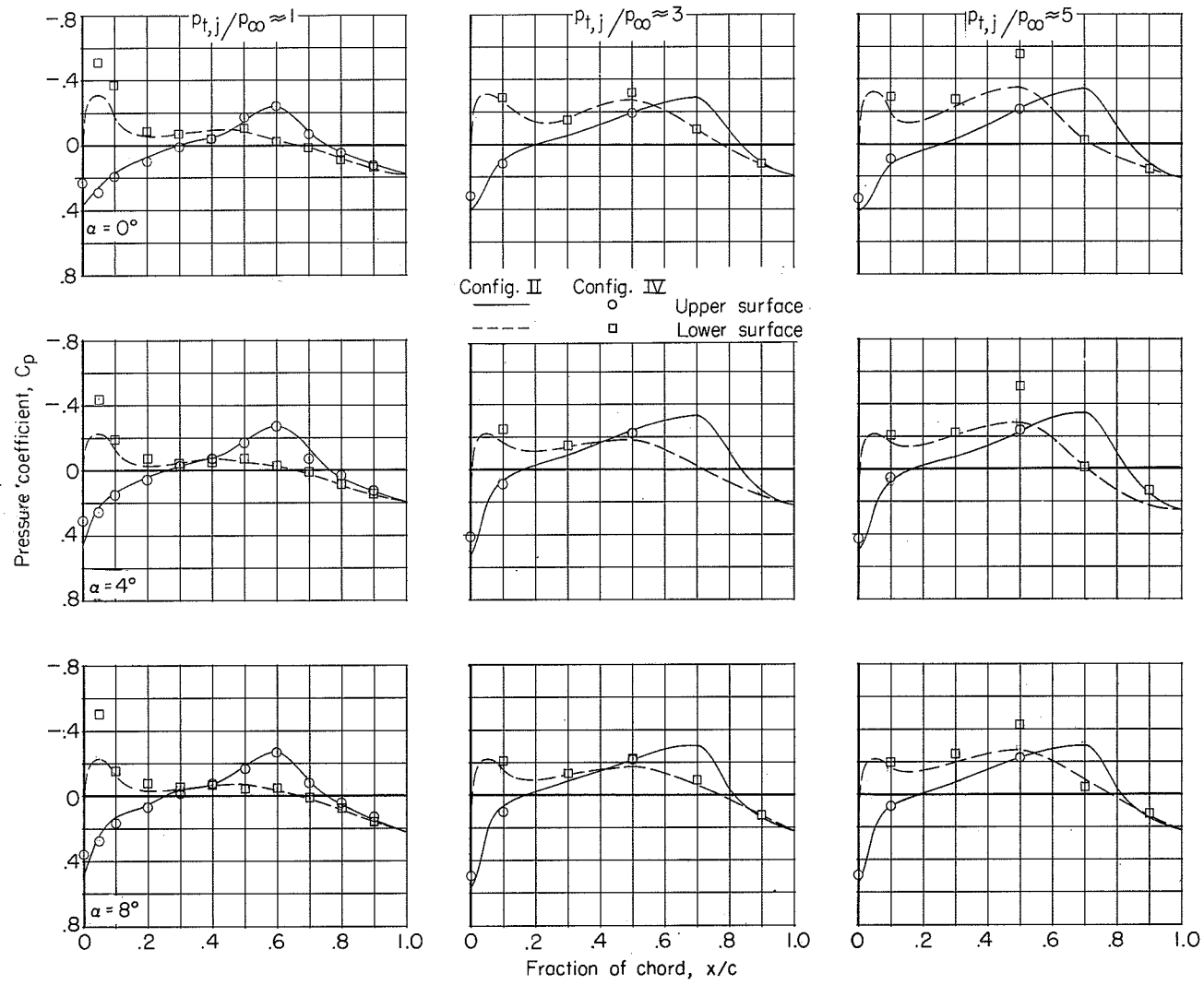

Figure 27.- Effect of engine exit location on horizontal-tail pressure distribution. Configurations II and IV; $M_\infty = 0.95$.

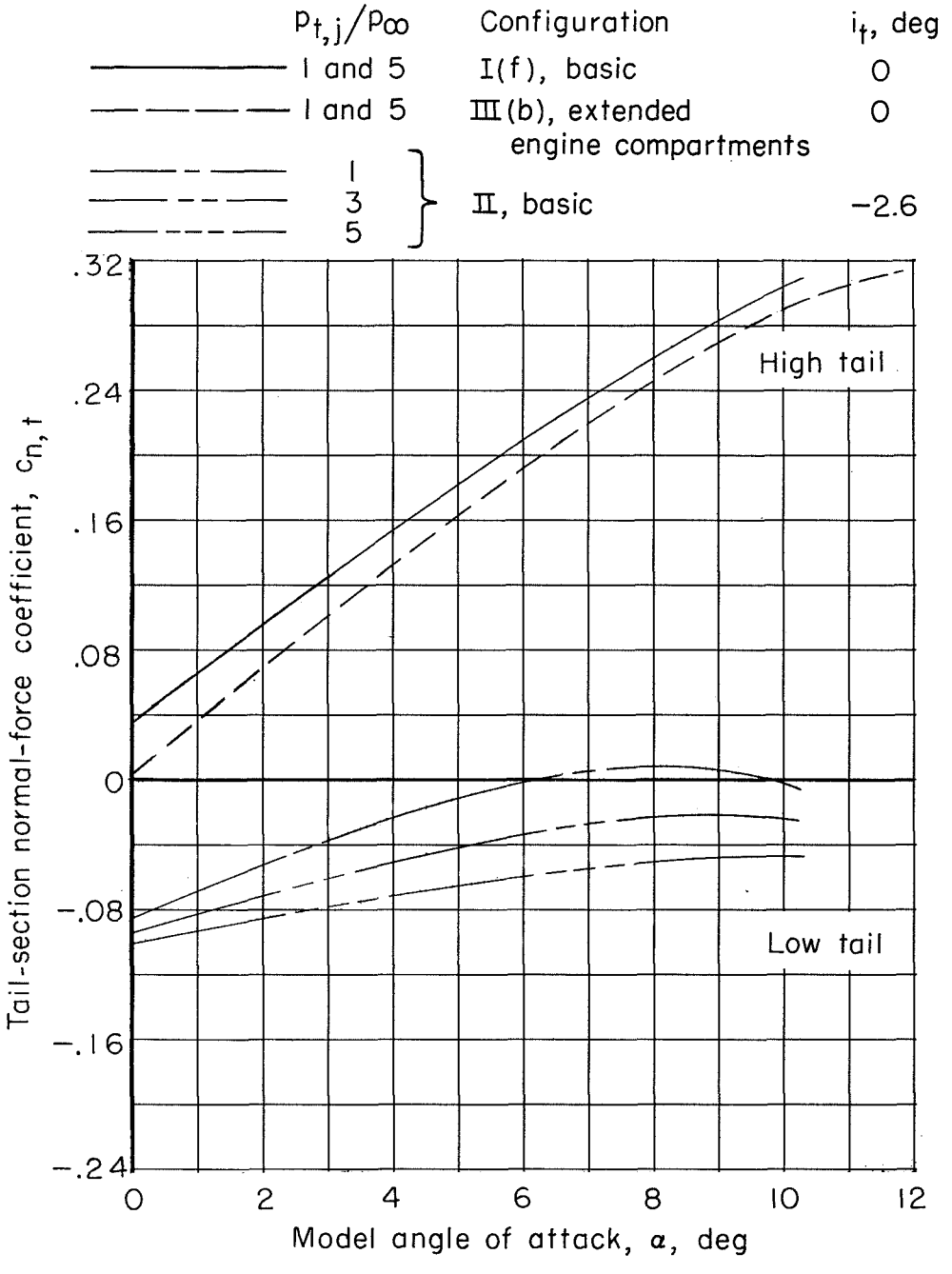

(a) $M_\infty = 0.85$.

Figure 28.- Variation of horizontal-tail section normal-force coefficient with angle of attack. Configurations I, II, and III.

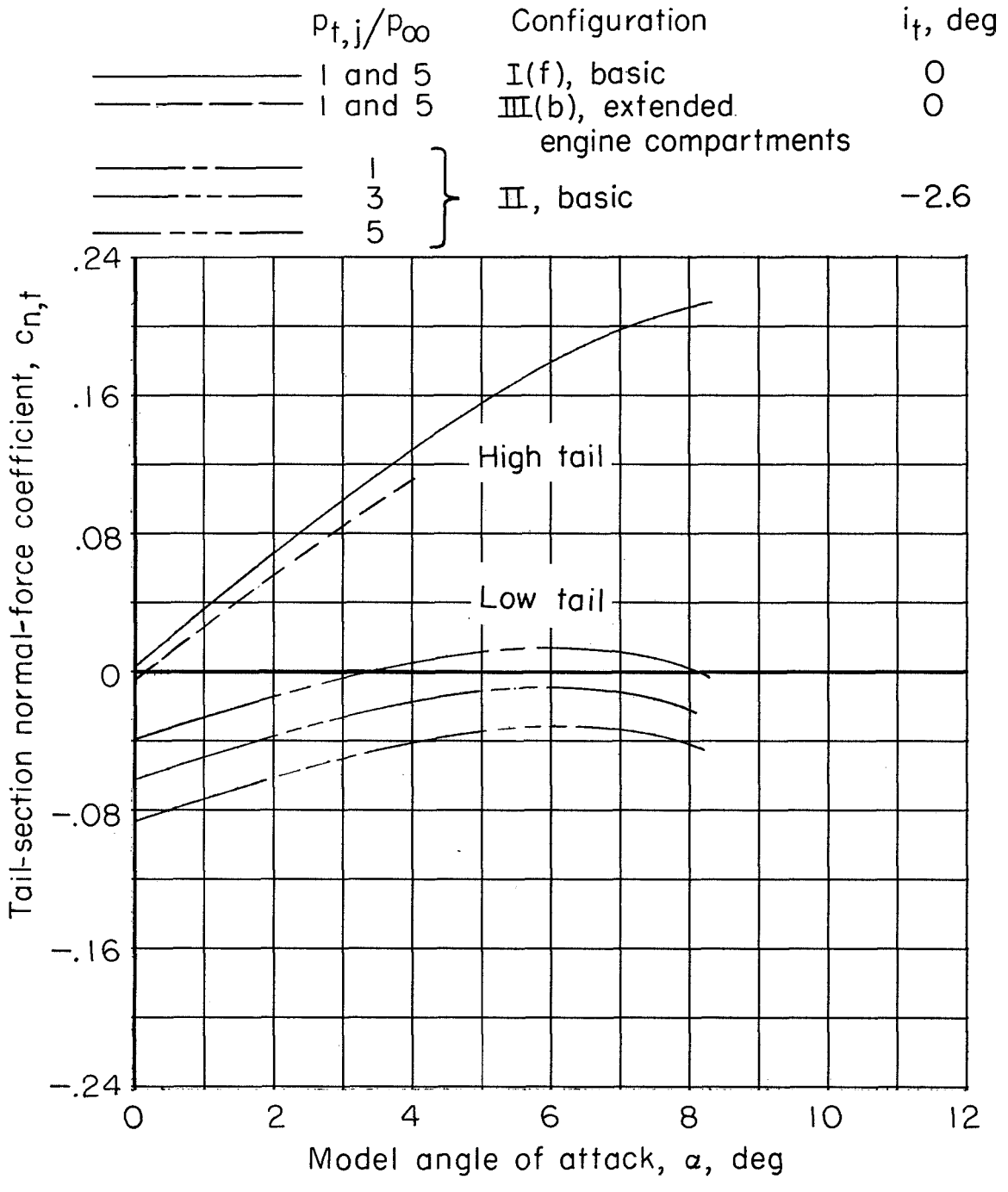

(b) $M_{\infty} = 0.95$.

Figure 28.- Continued.

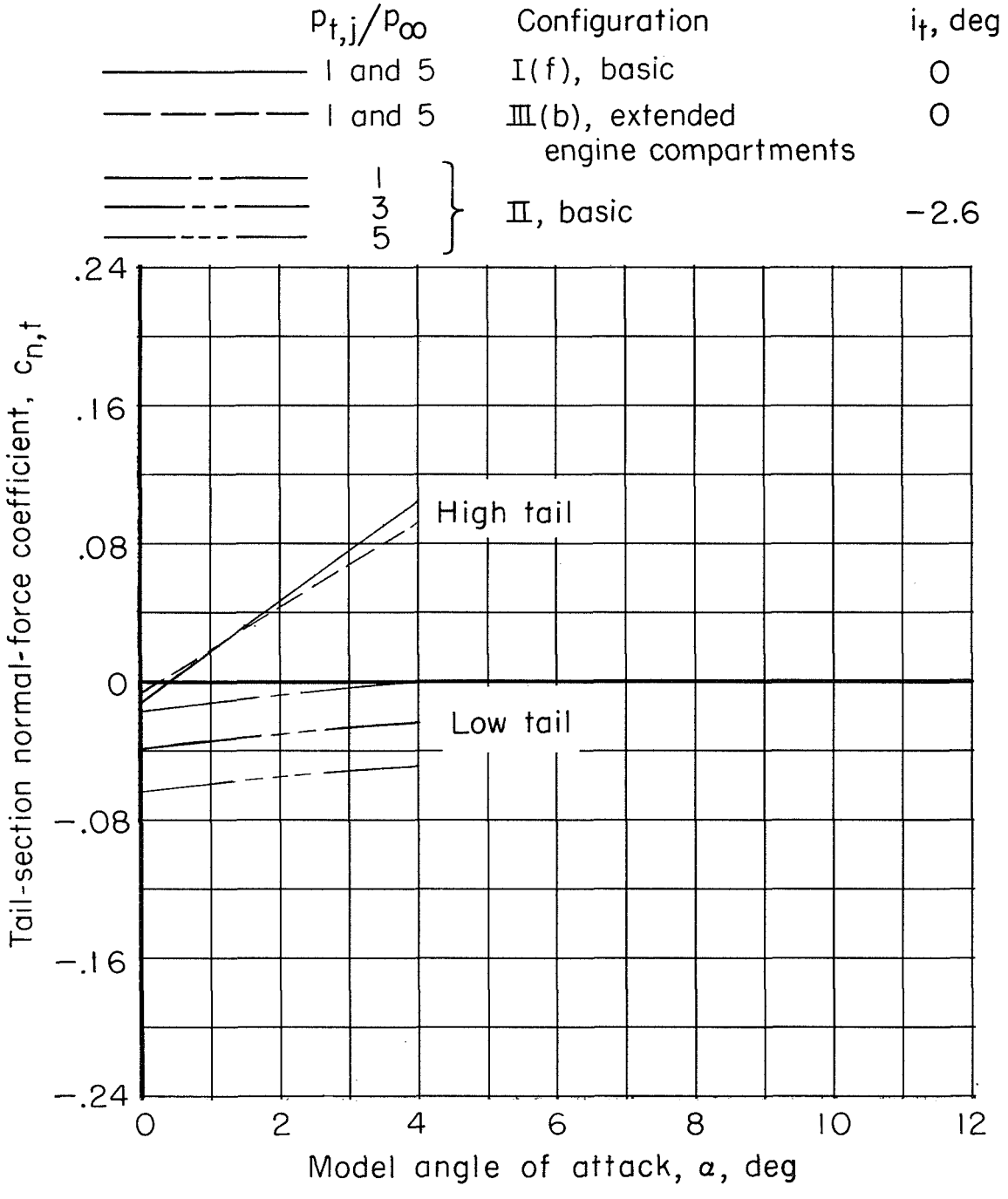

(c) $M_\infty = 1.00$.

Figure 28.- Concluded.

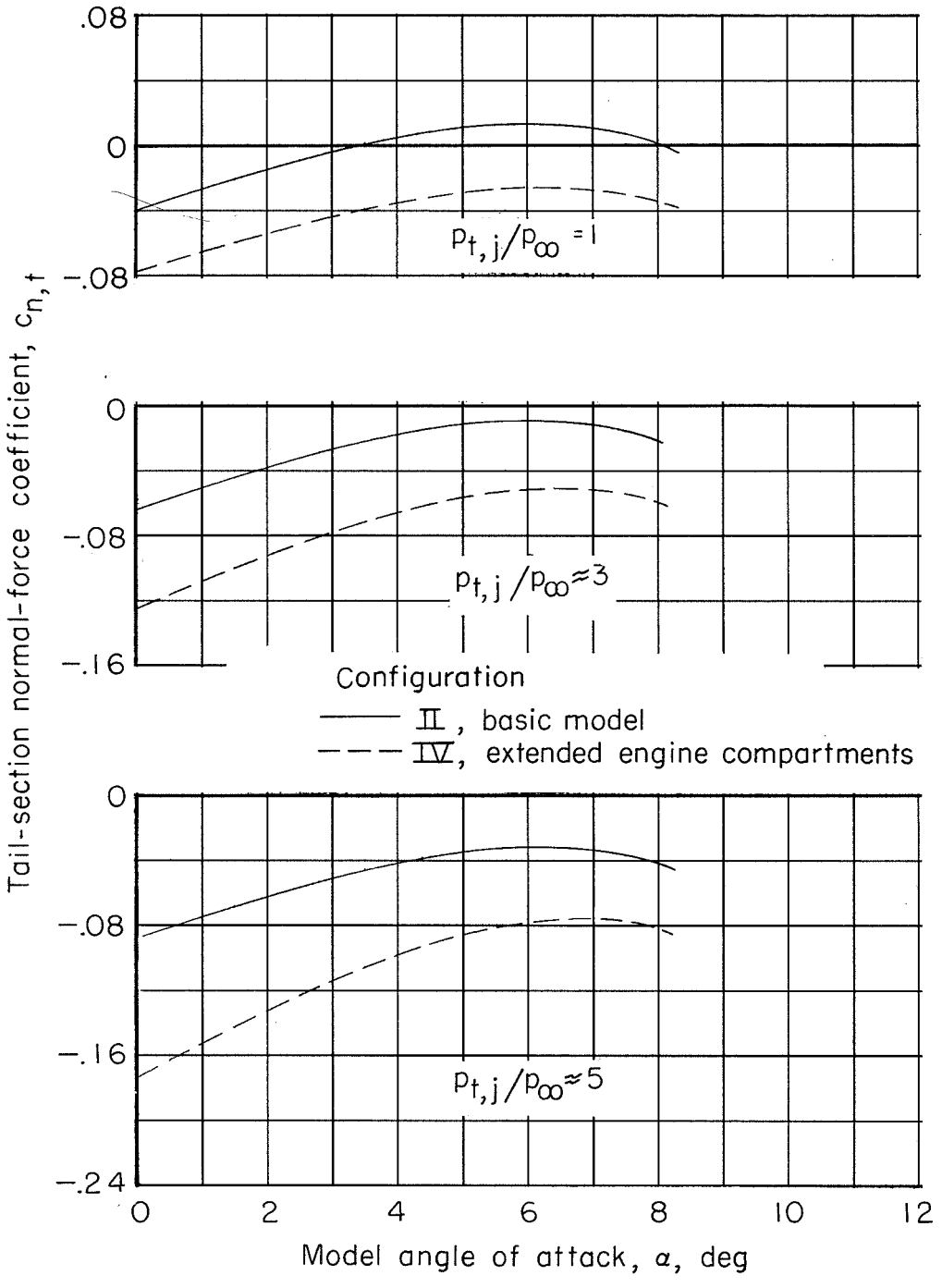

Figure 29.- Effect of engine exit location on horizontal-tail section normal-force coefficients. Configurations II and IV; low horizontal tail; $M_\infty = 0.95$.

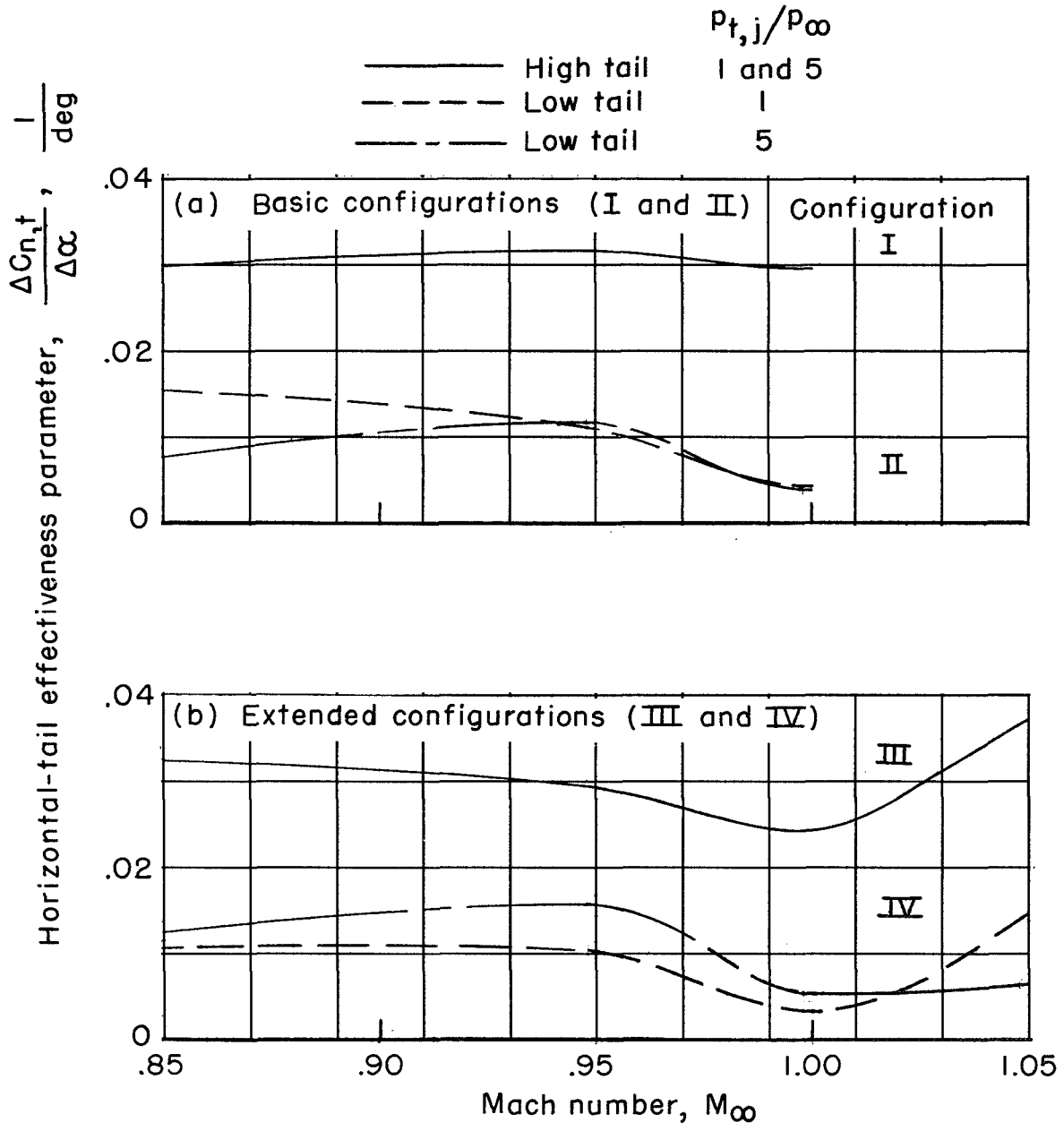

Figure 30.- Variation with Mach number of the horizontal-tail section effectiveness parameter.

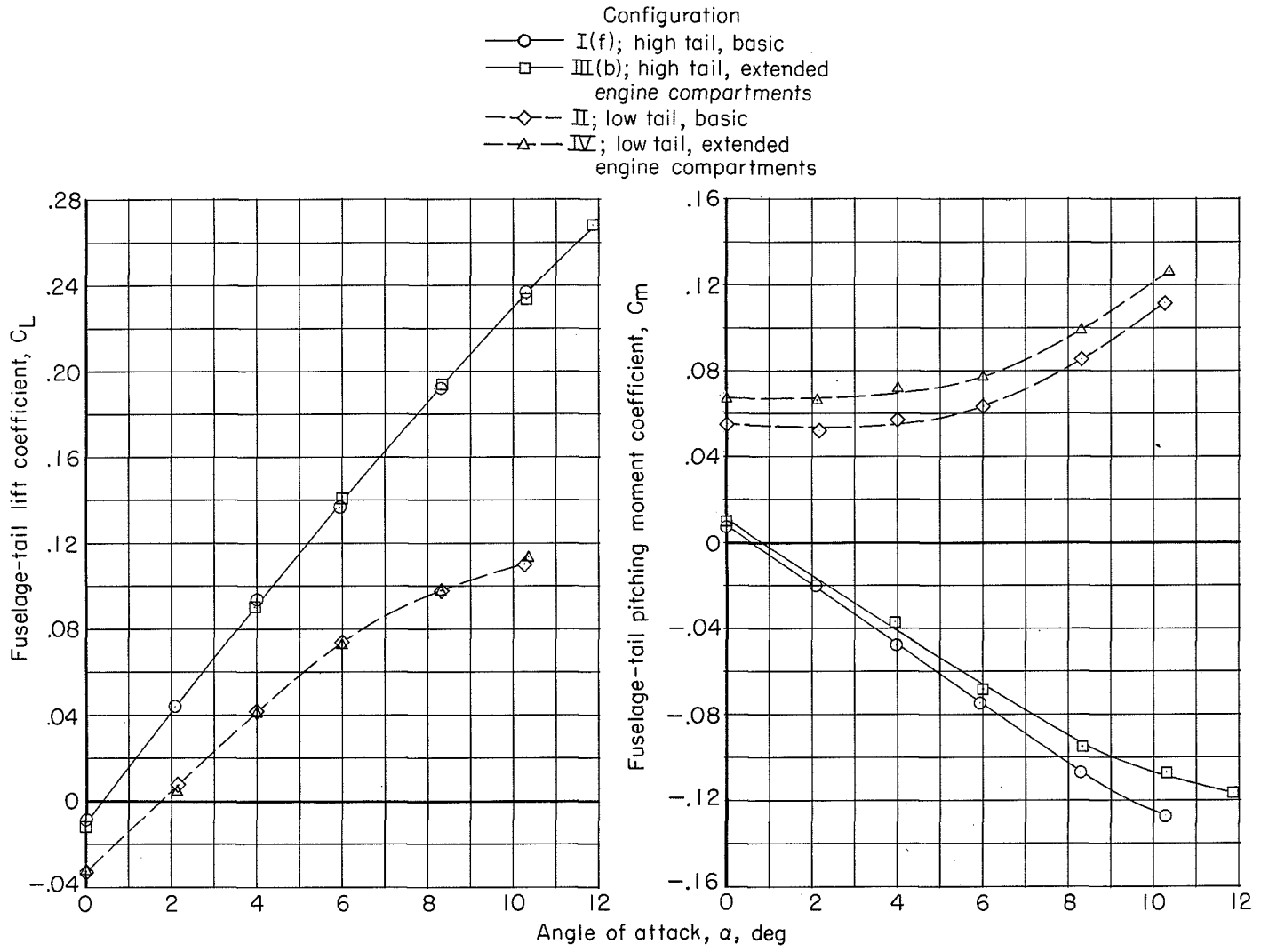

Figure 31.- Variation of fuselage-tail lift and pitching-moment coefficient with angle of attack. $M_\infty = 0.85$; jets off.

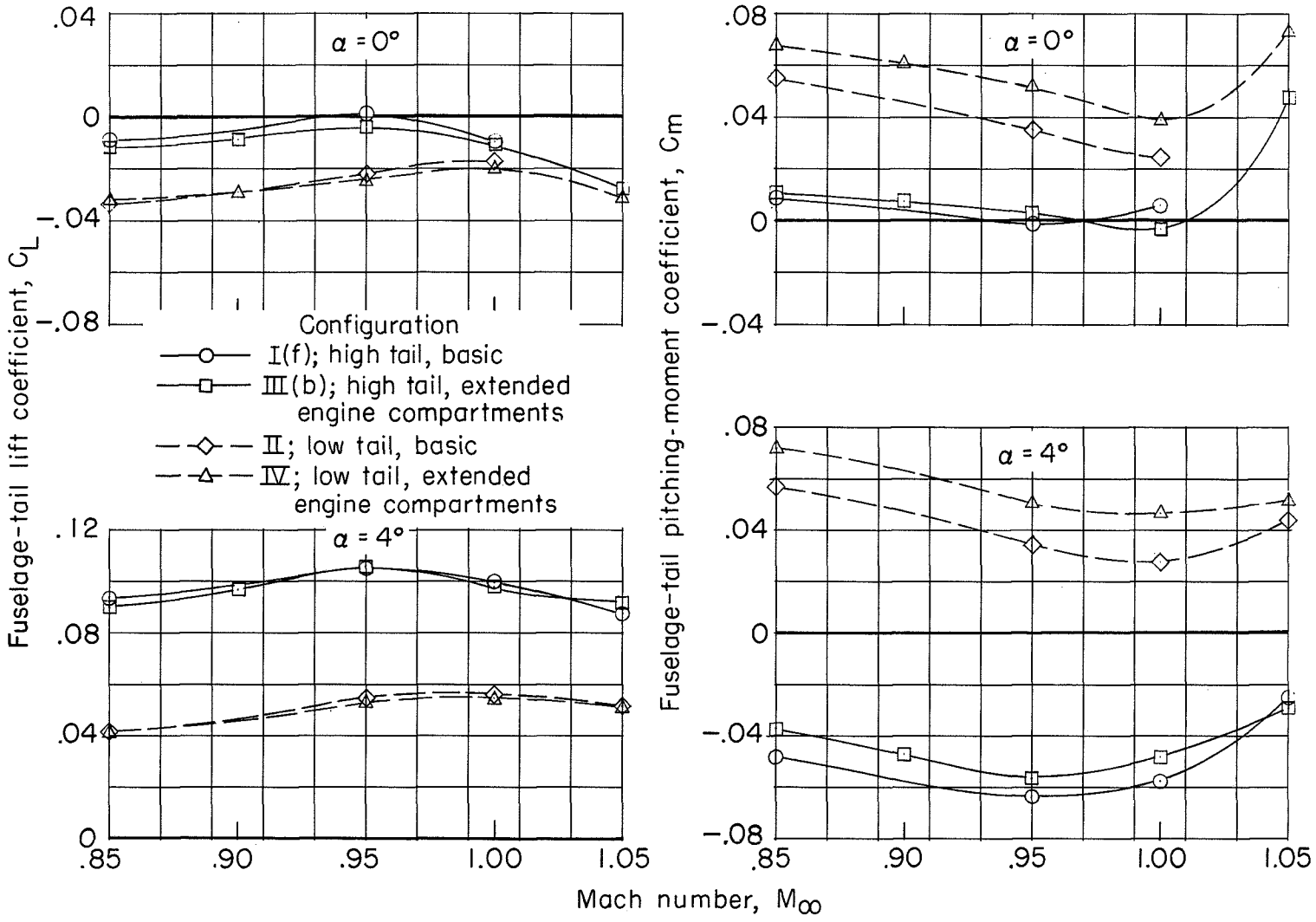

Figure 32.- Variation of fuselage-tail lift and pitching-moment coefficients with Mach number. Jets off.

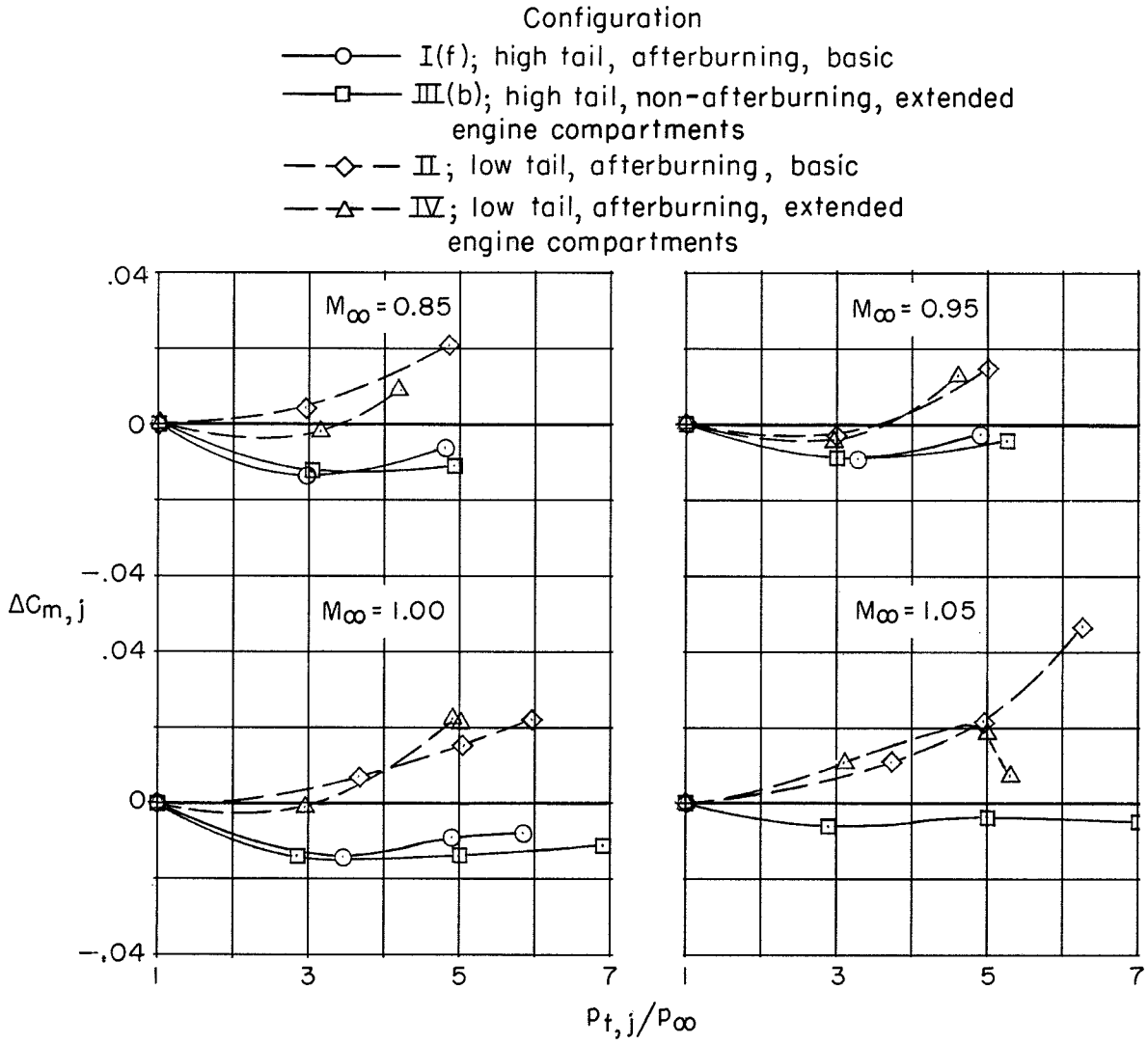

Figure 33.- Incremental pitching-moment coefficients due to jet operation. $\alpha = 4^\circ$.